Chapter 4

Microfluidics for Small-Angle X-ray Scattering

Serena A.J. Watkin, Timothy M. Ryan,
Antonia G. Miller, Volker M. Nock,
F. Grant Pearce and Renwick C.J. Dobson

Additional information is available at the end of the chapter

http://dx.doi.org/10.5772/65678

Abstract

Small-angle X-ray scattering is a well-established biophysical technique, whilst microfluidics is proving to be a convenient technology for creating miniaturised multifunctional devices. Both fields are highly versatile and find use in multiple scientific disciplines. Together, they offer the potential to obtain structural information on biomacromolecules, nanoparticles and condensed matter, in a high-throughput manner and with enhanced time-resolution capabilities. This chapter provides practical design considerations for X-ray-based microfluidic systems and examines some of the existing microfluidic platforms used in conjunction with small-angle X-ray scattering. As the exclusive advantages of microfluidics become recognised and accessible, the prevalence of microfluidic sample environments in X-ray scattering measurements will hopefully increase.

Keywords: microfluidics, high throughput, time-resolved SAXS, continuous flow, laminar flow, hydrodynamic focusing, turbulent mixing, structural biology

1. Introduction

1.1. Principles and potential of microfluidics

The interdisciplinary field of microfluidics encompasses the science and technology underlying the development of devices that process and manipulate small volumes of fluids within micron-scale channels. A microfluidic 'chip', so-called because its fabrication method was adapted from that used to manufacture computer microchips [1], can be designed with interconnected networks of channels and chambers. These designs can integrate a range of

functions on a single, microsized 'lab-on-a-chip' device, also known as a 'micro total analysis system' (μTAS). Along with the ready possibility of automation and potential for high-throughput screening that microfluidics presents, other general benefits of scaling down include lower sample consumption and consequently lower cost. In addition, microfluidic devices offer precise control over fluid flow and mixing, shorter processing times and hence more rapid results. Accordingly, the technology of microfluidics is influencing many areas of science, from materials to microbiology.

1.1.1. Physics of fluid flow on the microscale

In contrast to fluids moving in large channels, which mix turbulently, a key property of fluid flow in microchannels is that it is laminar. Laminar flow occurs in smooth parallel streams with no significant mixing between streams other than by diffusion [2]. This is a result of the ratio of inertial to viscous forces, described by the Reynolds number (*Re*), which for small channel dimensions is low, meaning that viscous forces dominate. The Reynolds number is defined by

$$Re = \frac{\rho v w}{\mu} \tag{1}$$

where ρ is the fluid density, v is the flow velocity, w is the characteristic dimension of the flow geometry and μ is the fluid viscosity [3]. A *Re* of <1–100 corresponds to pure laminar flow, whilst a Re of >1000–2000 is approaching turbulent flow. The low Reynolds number flow property of microchannels can be exploited, but is not ideally suited to all applications.

1.2. The combination of microfluidics and small-angle X-ray scattering

Small-angle X-ray scattering (SAXS) is a valuable and versatile technique. SAXS is utilised by biochemists and material physicists alike, providing both quantitative and qualitative structural information about biomacromolecules, nanoparticles and condensed matter [4–13]. In structural biology, although SAXS is unable to afford atomic resolution, it serves as a complementary technique to X-ray crystallography and nuclear magnetic resonance (NMR) and compensates for limitations of these techniques, by enabling structural parameters to be determined in biologically relevant solutions, without the size restriction typically imposed by NMR and with no requirement for extrinsic biomolecule labelling or crystals. Further, SAXS allows the characterisation of conformational changes, dynamics and interactions of biomolecules in response to different experimental conditions, which makes it ideally suited to monitoring important biochemical events, such as protein folding, ligand binding and association/dissociation reactions.

1.2.1. Why incorporate microfluidics into SAXS?

SAXS already involves the manipulation of relatively small volumes of fluid; however, the typical solution sample environment for SAXS is based on thin-walled quartz capillaries. These offer a convenient method to acquire SAXS data on solutions, but they do have a number of

http://dx.doi.org/10.5772/65678

restrictions. Microfluidic devices offer the opportunity to develop customised systems with the flexibility to enable advanced sample handling, such as concentrating, diluting, mixing and filtering, in line with the SAXS measurement. Unsurprisingly, given its broadly applicable advantages, microfluidics has been incorporated into several other techniques in assorted scientific fields and within structural biology, including for screening of protein crystallisation conditions, for a closely related technique, X-ray crystallography [14], and with few perceivable disadvantages, the question really becomes, why not SAXS? Indeed, several groups have already recognised the potential benefits and taken advantage of microfluidics, successfully demonstrating its use with SAXS for studying a diverse variety of specialised systems [12], including the assembly of biomacromolecules such as intermediate filaments [15] and silk fibres [16]; the growth of gold nanoparticles [17]; the rheology of complex fluids, such as liquid crystals [18, 19] and wormlike micelles [20]; as well as numerous studies on protein [21–29] and RNA folding [30, 31]. Perhaps the most obvious, more general advantage that microfluidics can offer SAXS, as it has offered many other techniques, is the potential to provide automated, high-throughput platforms which minimise sample consumption and shorten measurement times whilst maintaining a high level of accuracy and reproducibility, and researchers have begun to lay the groundwork for devices of this type [32–34].

1.2.2. What makes microfluidics particularly well-suited to SAXS?

Several fundamental aspects of these technologies are exceptionally compatible. First, the size of the X-ray beam relative to the size of the channels within a microfluidic chip is quite comparable. Thus beam is not being used to measure extraneous material, and conversely, all of the sample molecules are in the beam interaction volume. Therefore the sample is providing the optimal amount of signal, without being wasted. Second, the continuous flow typical within these systems mitigates radiation damage to samples, improving the reliability and data quality obtainable from SAXS measurements. Moreover, the high-throughput potential mentioned above is especially important for synchrotron-based techniques such as SAXS, where the experiment time is often limited, as a microfluidic sample-handling platform could help to ensure maximum use of the allocated beam time [33, 35]. This is what prompted Lafleur et al. and, very recently, Schwemmer et al., to develop their respective microfluidic high-throughput sample-handling environments [33, 34], which will be discussed. Microfluidics also offers the opportunity to extend the time-resolution capability of SAXS. Various groups have demonstrated the possibility to study reaction kinetics of protein and RNA folding events or complex fluids, using alternative microfluidic approaches to prevail over commercially available stopped-flow devices which fall short of the requisite microsecond time range, and this will be covered in the latter part of this chapter.

2. Incorporating microfluidics into SAXS

In the first part of this section, some general design considerations for microfluidic systems in the context of SAXS will be discussed. In subsequent sections, existing examples of microfluidic chips and how they have been applied using SAXS in order to increase either the throughput

or the time resolution will be examined. As well as providing some background and giving an overview of the current status of the field, it is hoped that this chapter will contain practical information for those looking to realise the benefits of incorporating microfluidic technology into SAXS.

2.1. Design considerations for SAXS microfluidic systems

Whilst the specifications of the system will differ depending on the particular application, some generally applicable guidelines are given here, supplemented with specific examples. As for any analytical microfluidic setup, there are three main aspects of the system which need to be considered: (i) the design and fabrication of the microfluidic chip itself, (ii) the sample delivery system and method of fluid control and (iii) integration with the experimental apparatus, in this case, the SAXS beamline (although the possibility of an on-chip X-ray source has been envisaged [36]). Each aspect will be discussed separately here whilst bearing in mind that these aspects are all interrelated and will have certain SAXS-specific requirements that differ from other light-based detection methods.

2.1.1. Chip design and fabrication

The first key consideration regarding the microfluidic chip is the choice of material, the properties of which, in this case, must be compatible with X-rays. The possibilities will be further narrowed down by practical considerations specific to the particular application, e.g. if high flow rates are required for mixing or time-resolution purposes, the chip material and bonding must be robust enough to withstand the subsequent high pressure generated, without deformation of the microchannels [20, 27]. Cost, both in terms of fabrication time and resources, will also likely factor into material choice, and the type of material will dictate the method of fabrication, which may be limited by available facilities. Microfabrication does require some special equipment and sometimes a clean room, commonplace in a nanofabrication facility, but not found in the average biochemistry lab. If access to the necessary facilities is not available, there are several microfluidic manufacturing companies offering custom microfabrication services.

Microfluidic chips were originally manufactured from silicon using standard photolithography and often bonded to glass, which is not an ideal window material for SAXS [36]. The first microfluidic device used in conjunction with SAXS comprised a silicon chip and silicon nitride windows [21], but in more recent times, silicon has been exchanged for synthetic polymer materials, such as thermoplastics, e.g. polymethyl methacrylate (PMMA), or the silicone elastomer, polydimethylsiloxane (PDMS). The latter is cast from a replication master mould, which can be fabricated using similar lithographic techniques, whilst the former can be fabricated by a range of micromachining methods (milling, electric discharge, laser ablation) and templating techniques (thermoforming, transfer moulding). Both options are cheaper than silicon chips and highly flexible in terms of the possible channel geometries.

Unfortunately, there are two major limitations of PDMS for microfluidic SAXS devices: its low X-ray transparency [36] and its low X-ray endurance—continuous X-ray exposure rapidly

http://dx.doi.org/10.5772/65678

deteriorates this material [20]. Nevertheless, PDMS can be utilised for channel structures, as long as appropriate X-ray compatible material is chosen for sample observation windows, as Dootz et al. demonstrated [19]. As another example, Stehle et al. used a PDMS chip for a microfluidic droplet-forming module, separate from the thin-walled glass capillary used for SAXS detection [12]. The large dead volumes that are introduced *via* the connecting tubing in this system are the disadvantage of this approach. PDMS also finds use in other constituents of a microfluidic system, as its elasticity and adhesive properties render it useful for valves and seals [33].

Kapton (polyimide) has commonly been used for X-ray-related applications due to its high X-ray resistance and low X-ray absorption [19]. However, in a qualitative assessment of the suitability of various polymer materials for SAXS microfluidic chips by Toft et al., the SAXS profile obtained from a 100 μm thick Kapton foil revealed a diffuse diffraction peak that occurs at in the middle of biologically relevant q-ranges [32]. Given that biological scattering is relatively weak, this feature was suggested to perhaps cause issues with background subtraction [32]. In spite of this, Barrett et al. have fabricated a microfluidic device out of two 150 μm thick Kapton films bonded together, using laser ablation techniques to produce the channels, whilst Graceffa et al. used Kapton windows for their stainless steel turbulent-flow mixing chip [27], as did Dootz et al. for their PDMS chip [19].

Greaves and Manz deemed polycarbonate (PC) to be the best chip-building material in terms of X-ray transmission, with PMMA a close second [36]; however, PC and PMMA were rated poorly by Toft et al., in terms of X-ray endurance and cleaning, and PC was also judged as poor for bonding and machinability, although both materials display low small-angle X-ray scattering [32]. Ultimately, polystyrene (PS) was the polymer of choice for Toft et al., meeting all the criteria for their 'BioXTAS' chip [32, 33], whilst Lafleur et al. selected PMMA for a mixing attachment containing rotary valves by virtue of its superior machinability [33]. Combinations of different plastics have also been demonstrated successfully by Møller et al., who used a PMMA substrate with PS windows, developing a strong PS to PMMA bonding procedure for this design [37].

A second, crucial consideration relating to SAXS chip design concerns the size of the sample detection compartments versus the size of the X-ray beam. For maximum signal, the depth of the sample compartment should be as close to the optimal pathlength as practically possible. The scattering volume and the beam energy both factor into determining the optimum pathlength. Conversely, using smaller compartments results in lower sample consumption. A finite constraint is that the dimensions of the beam must be smaller than the dimensions of the channel or chamber to minimise background intensity resulting from X-ray interaction with the substrate wall, and the X-ray focusing or slitting down ability and resultant flux of individual beamlines will set a lower limit on these dimensions. It is important to note that the beam dimension under consideration is the total beam width, as opposed to the commonly defined full width at half maximum, as the weak outer beam background will still cause parasitic scattering from the chip which will affect data quality. Thus the design must be optimised to the expected beam dimensions and balance signal requirements against sample consumption.

2.1.2. Sample input and fluidic control

For continuous flow systems, fluid delivery *via* pumps would ideally be controlled remotely by software, so as to facilitate fast sample turnover time and minimise the need to access the beamline hutch, thereby increasing the efficiency of the experimental procedure. This is essential for time-resolved measurements, where data acquisition must be initiated immediately after sample mixing. Toft et al. developed software to couple control of commercial syringe pumps delivering samples and buffer to the chip with the beamline shutter system, thereby coordinating sample preparation and data collection [32], whilst Lafleur et al. developed both the software and hardware, including the individually controlled syringe pumps used in conjunction with integrated rotary valves, for their next-generation setup [33]. For stopped-flow systems, sample introduction to the chip and any on-chip processes such as mixing, diluting could be done prior to chip introduction to the beamline, provided that time-resolved data are not required. Alternatively, Schwemmer et al. eliminate the need for pumps and tubing altogether (along with any associated plumbing problems) by depositing samples directly into reservoirs on their 'LabDisk' using regular pipettes. This keeps all fluids confined entirely to the chip and relies on centrifugal forces to transport fluids through the mixing channels, though this does require a custom-built processing device to spin the disk at preset rotational frequencies [34].

2.1.3. Interfacing to a SAXS beamline

Once the chip is fabricated and fluidic control is established, the final considerations to complete the microfluidic SAXS experimental setup and ensure optimal ease of use involve appropriate interfacing to the beamline. This may require some adjustments to the conventional beamline setup to accommodate the microfluidic system. At a minimum, a chip holder, which allows for any necessary inlet and outlet tubing connecting to the fluid delivery system, is needed for stable attachment to an adjustable stage (ideally motor-controlled) to facilitate precise alignment with the X-ray beam. More advanced chip holder designs have included a borescope or camera for sample visualisation and to assist with chip positioning [34, 37]. For the best-quality data, the beamline setup should ensure a vacuum along the complete X-ray flight path, from synchrotron to microfluidic sample chip to detector to avoid air scatter, and contain a minimum of extra window components to reduce background intensity [34]. Temperature control is another important consideration, particularly for unstable biological samples, and has been achieved *via* a channel in the chip holder through which a cooled solution can be passed [37].

2.2. Microfluidics for high-throughput SAXS sample handling

Prior to the development of sample-changing robots at synchrotron SAXS beamlines, loading samples by hand was a tedious and time-consuming process, especially with the necessary sample cell cleaning and drying steps between each sample [35]. This motivated Toft et al. to develop a microfluidic front end, the BioXTAS chip, along with software for external control of the syringe pumps regulating fluid flow through the chip [32]. At the time, this was a considerable improvement upon manual sample handling, with the added benefit of elimi-

http://dx.doi.org/10.5772/65678

nating the inherent human error associated with sample preparation, such as that of a dilution series, which is generally still a manual task, at present. The first-generation BioXTAS chip (**Figure 1A**) contained four fluidic inlets, providing the option to utilise up to three different solutions that are premixed prior to merging with the sample solution, an extended serpentine mixing channel in which homogenous mixing of sample and buffer solutions occurs *via* diffusion, with the mixing ratio determined by the flow rate, and a 200 nl sample chamber, where the sample is exposed to the X-ray beam and scattering data is collected whilst flow is stopped [32]. In this setup, samples are stored in syringes connected to the chip by a 30 cm length of tubing which requires 150 μl of solution to fill, and following a 15 min pressure-equilibration period, 6 min is required to fill the sample chamber, at a flow rate of 6 μl/min [32]. Consequently, whilst only 36 μl of sample is consumed per measurement, and reasonable quality data has been shown from a mere 200 nl sample volume (of 1–10 mg/ml protein), unfortunately this sample economy is compromised by the dead volume contained in the syringe and tubing, as well as by the pressure-equilibration time. Although the stopped flow during data collection strategy contributes to low sample consumption, it does increase the susceptibility of the sample to radiation damage, particularly with long exposure times. Nevertheless, this BioXTAS chip represents a respectable first proof of concept of a microfluidic alternative for SAXS sample handling and has subsequently been utilised for a study on the oligomeric state of cancer-related protein, as further demonstration of its practicality and promise [37].

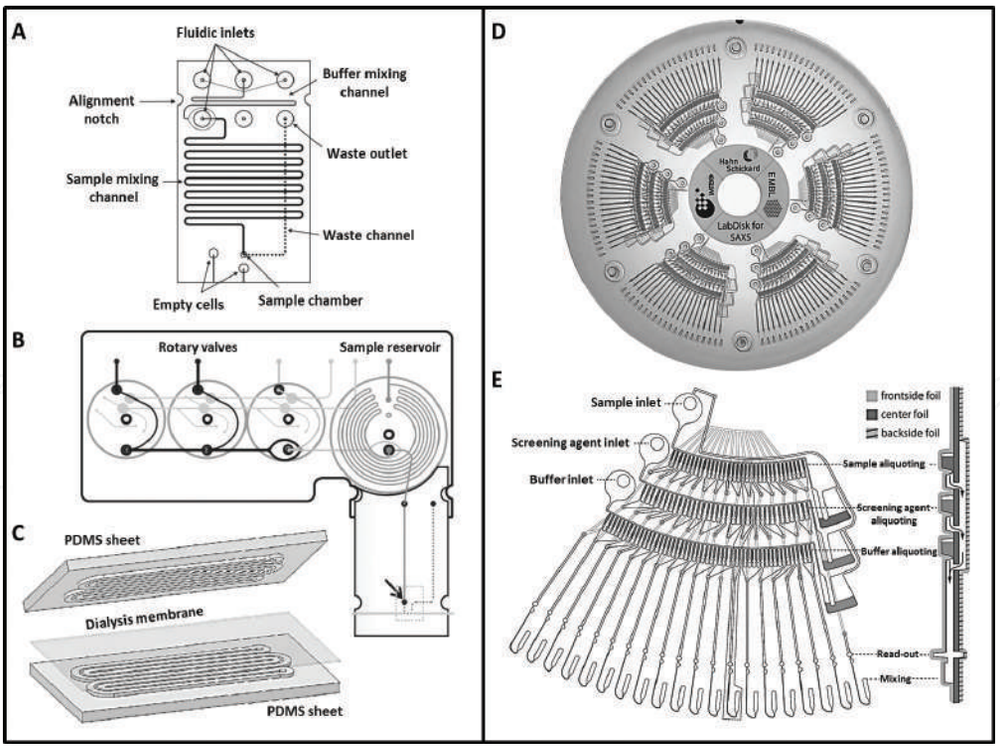

Figure 1. Microfluidic answers to the demand for automated, high-throughput, low consumption sample-handling systems for SAXS. (A–C) The BioXTAS chip by Toft et al. [32] and additions by Lafleur et al. [33] and Skou et al. (2014) [38]. (D and E) The LabDisk for SAXS by Schwemmer et al. [34]. See text for details.

The first-generation BioXTAS chip was subsequently developed to incorporate an additional mixing module (**Figure 1B**), which contains an on-chip sample reservoir and motor-controlled rotary valves to enable more precise fluidic control, in addition to integrated UV absorbance detection capabilities by means of optical fibres built into the separate sample detection chip, enabling UV absorbance measurements to be acquired concurrently with scattering data [33]. The option for data acquisition in continuous flow mode, which would reduce radiation damage, albeit at the expense of sample consumption, is made available in the custom-developed control software [33]. With much shorter exposure times on a more powerful X-ray source and a faster flow rate, the complete experimental cycle time (including cleaning) was considerably reduced from 28 to 3 min whilst consuming slightly less sample than for the first-generation chip [32, 33]. The on-chip sample reservoir does enable a reduction in the dead volume of the system, although external syringe pumps and associated tubing are still required to supply the buffers and pressure on the protein sample, so in order to take full advantage of the on-chip reservoir to minimise the sample volume, the suggestion is made to use an immiscible fluid to supply the necessary volume in the tubing syringe for injecting the sample [33].

Related to this idea of introducing a second fluid phase is the droplet-based microfluidic approach, in which discrete droplets of one liquid are generated, dispersed in and carried by a second, immiscible fluid within a microchannel [12]. These microdroplets can be used to compartmentalise samples, which can then be manipulated as individual vessels: for sorting, splitting, merging and even for performing chemical or biological assays [12]. The usefulness of this approach in association with SAXS was demonstrated by Stehle et al., who used it to analyse gold nanoparticles encapsulated by water droplets dispersed in oil, with each SAXS measurement comprising data averaged from ~ 9000 droplets, over a 15 min period [12]. In view of the available sample-changing robots, which have similar sample requirements and low dead volumes and perform all of the necessary cleaning in a fully automated fashion, distinct advantages of microfluidic devices for SAXS may have thus far been unclear, whereas discrete droplet formation is an example of an exclusive capability of microfluidic approaches which highlights the versatile possibilities created by this technology and which the standard SAXS setups lack. Another example is provided by Skou et al., who adjusted the second-generation BioXTAS design to incorporate a sample dialysis chip, comprising two PDMS sheets: one which contains channels for a polyethylene glycol (PEG) solution and the other which contains channels for the protein sample solution and a dialysis membrane sandwiched in-between (**Figure 1C**) [38]. When utilised with SAXS, this additional microfluidic module offers the unique ability to gradually concentrate protein samples as structural information is continually acquired, to reveal changes in protein oligomeric state and detect concentration-induced protein aggregation early in the experiment. Alternatively, if a different buffer is used instead of a PEG solution, the device can be used to monitor the effect of different experimental conditions, such as a change in ionic strength or pH, during buffer exchange [38]. Further advanced sample-handling features envisaged for microfluidic SAXS include on-chip size exclusion chromatography [32].

Although the BioXTAS chip readily facilitates mixing of multiple solutions with small volumes of a single sample and prepares dilutions with ease (simply by varying the flow rate), in order to properly meet the high-throughput objective, the BioXTAS system would require further development to increase its sample capacity or the means to enable easy and rapid sample changing, to bring it up to par with current autosampler robots. Schwemmer et al. presented an innovative centrifugal microfluidic platform, 'LabDisk for SAXS', which overcomes some of the shortcomings of the BioXTAS system by having six sample modules on a single chip (**Figure 1D**), each containing on-chip reservoirs for sample, buffer and screening agents and requiring only 2.5–3.5 μl of solution, with dead volumes of just over 1 μl, which is the allowance for pipetting errors and guaranteeing complete filling of channels and chambers [34]. The sophisticated fluidic geometry (**Figure 1E**) enables aliquoting and mixing of fixed combinations of protein, buffer and screening agents, simultaneously generating 15 different sample conditions and the five corresponding buffer solutions for background subtraction, with a high degree of accuracy and precision, in under 5 min [34]. Short (20 × 50 ms) exposures make for fast readouts, with the experimental time currently limited by manual positioning of the measurement chambers in the X-ray beam, although this is expected to be automated in due course [34]. Higher noise in the data collected on the LabDisk than the conventional sample changer is attributed to factors relating to the air gap in which the LabDisk is operated, which results in higher background, as well as the shorter pathlength of the measurement chamber and smaller X-ray beam, which result in lower signal [34]. Owing to the relatively low signal of biomolecules, composed of light, weakly scattering atoms, the background subtraction, which accounts for both the solvent and the instrumentation, needs to be carried out as precisely as practically possible. As such, the use of the same sample compartment for both sample and background measurements is considered important, to avoid introducing anomalies due to subtle differences in sample cell [35]. However, the LabDisk has separate readout chambers for samples and buffers, which has potential to cause issues with background subtraction.

2.3. Microfluidics for time-resolved SAXS

The suitability of microfluidic devices for time-resolved studies was recognised early on in the rise of microfluidics, and it has played a key role in increasing the time resolution attainable by SAXS. Whilst stopped-flow techniques have been extensively used for time-resolved SAXS studies, predominantly of protein folding [39–45], since Moody et al. reported the first device used in conjunction with SAXS in 1980 [46] and stopped-flow apparatus specifically for SAXS are commercially available [13], these have only been able to achieve dead times of 0.5 ms at best. Microfluidics offers the potential to extend the accessible time resolution of SAXS to the microsecond time range; however, rapid mixing, which is a crucial requirement, is the challenge, due to the low Reynolds number flow in microchannels.

The two main microfluidic approaches are both continuous flow-based techniques but differ in their mixing strategy; the turbulent-flow approach aims to generate high Reynolds number flow in microchannels, whilst the laminar-flow approach utilises the inherent low Reynolds number flow. The common underlying principle is that data collected at different distance

points along an observation channel after mixing correspond to different time points over the course of the reaction, with the flow velocity determining the temporal resolution. This approach has been coupled with various techniques, such as circular dichroism and fluorescence spectroscopy [29], but with SAXS, the radius of gyration represents an easily determined parameter which can be monitored, whilst the data also provide low-resolution structural information, making it useful for monitoring structural changes such as folding, oligomerization and ligand-induced rearrangements. As previously mentioned, continuous flow offers the SAXS-specific advantage of lower radiation damage but disadvantage of higher sample consumption, particularly at the high flow rates required for the turbulent mixing approach.

Rapid turbulent mixing in a multicapillary device was pioneered by Regenfuss et al. [47], who credits Moskowitz and Bowman [48], and this idea has since been developed by several groups, with various devices emerging [49, 50], including microfabricated versions of the original capillary-based mixer [51, 52]. The 'T-mixer' produced by Takahashi et al. [51] (**Figure 2A**) was subsequently utilised with SAXS to study the folding dynamics of various proteins [23–26, 31], achieving dead times as low as 160 μs [23]. The T-shaped geometry of this microfluidic device forces two solutions flowing at high velocities to meet at a junction and change direction, resulting in rapid mixing, before being transported through to the observation channel, where measurements are obtained [51]. Bilsel et al. advanced this design by altering the angle of the input channels such that they form an arrow-shaped junction (**Figure 2A** inset), which forces the two fluids to undergo a greater change in momentum, theoretically giving rise to more efficient mixing [52]. Using a device of this type, with channel widths of 75 μm, at a flow rate of 10 ml/min, the Reynolds number is calculated to be 2000, and the mixing time was demonstrated to be ~50 μs [52]. For time-resolved SAXS studies of protein folding, the dimensions of the observation channel were increased to 100 μm wide by 400 μm deep to increase the signal to noise, whilst the width of the input channels and mixing region was 30 μm, resulting in a dead time of ~100 μs at flow rates of 10–20 ml/min [27] (**Figure 2B**). Whilst these microfluidic setups are impressive in terms of the time resolution they can achieve, their major drawback is the large sample quantities necessitated by the high flow rates.

The laminar-flow-based rapid-mixing approach, introduced by Knight et al. in 1998, is referred to as 'hydrodynamic focusing' [53]. This approach relies solely on diffusive mixing, without introducing turbulence, taking advantage of the natural mixing process in microfluidic chips that function at low Reynolds numbers. For the hydrodynamic focusing geometry, two input fluids approach a central input fluid from either side, squeezing the central fluid into a thin, focused stream, across which diffusion occurs on a relatively short timescale [21, 53]. SAXS investigations of protein and RNA folding have subsequently been carried out using this type of device [21, 22, 30], achieving a minimum dead time of 240 μs [22]. This is a significant improvement on stopped-flow devices, but has not been improved further to match turbulent-flow mixers, at least, not in combination with SAXS. The hydrodynamic focusing approach for time-resolved SAXS is substantially limited by the size of the X-ray beam, as in order to access shorter timescales, the focused stream must be made even narrower; however, without the matching ability to adequately focus the X-ray beam, the system will suffer from low signal to noise. To complicate matters further, even if the beamline optics allow adequate microfocus-

http://dx.doi.org/10.5772/65678

sing, radiation damage to the slowly flowing sample becomes a particularly severe issue. Hydrodynamic focusing has been used with alternative detection methods [54], which have been able to accomplish mixing times as short as 10 μs [55], demonstrating the potential of this microfluidic approach for time-resolved measurements and providing incentive to work towards optimising optical designs of future SAXS beamline setups to overcome current technical barriers and take full advantage of it.

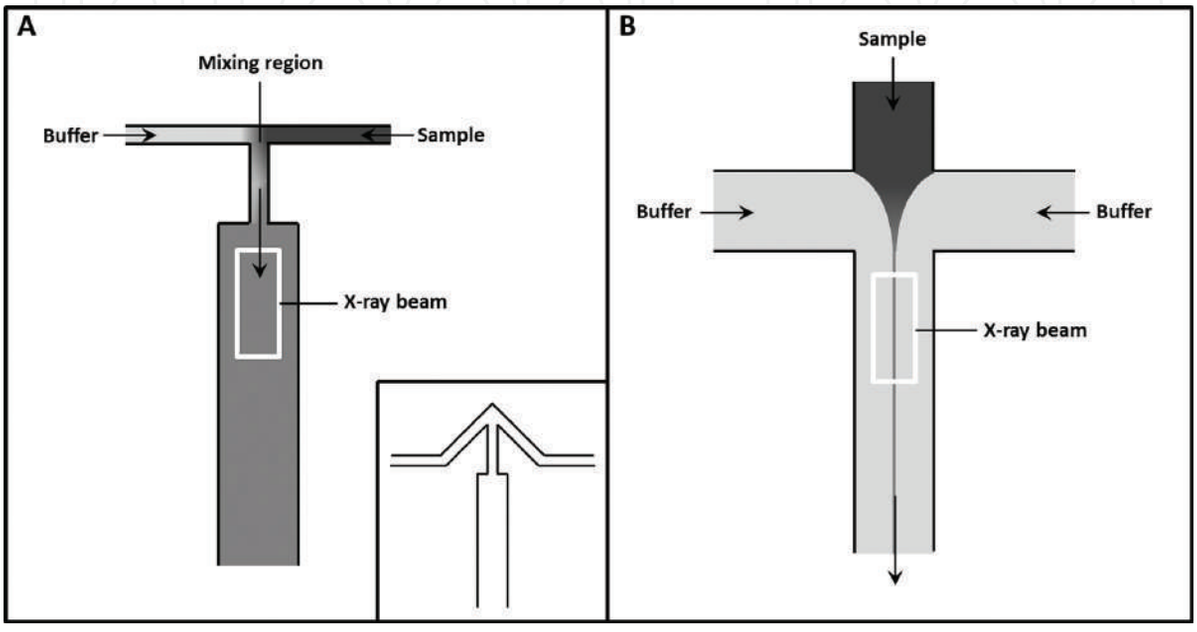

Figure 2. Two alternative rapid-mixing approaches in microfluidic channels for time-resolved SAXS. (A) Turbulent-flow mixing using the T-mixer [23] and arrow-shaped geometry [27] (inset). (B) Laminar-flow hydrodynamic focusing [21].

3. Conclusions and outlook

Over the last two to three decades, since microfluidics arose, various groups have recognised the advantage offered by this miniaturised technology and have successfully demonstrated its incorporation with SAXS. In particular, its high-throughput sample-handling potential and time-resolution–enhancing abilities have begun to be exploited. However this is still an emerging field, and microfluidic technology continues to push the boundaries and open up new possibilities, some likely yet to be conceived. With the current technology, 100 μs time resolution for SAXS studies on protein folding has been achieved. Although the turbulent- and laminar-flow mixers discussed above have been the most popular microfluidic approaches thus far, others have been looking to develop new mixing strategies, which could reduce dead times further, whilst the development of smaller, more highly focussed X-ray beams will be key to accessing faster timescales.

Author details

Serena A.J. Watkin[1,3], Timothy M. Ryan[2], Antonia G. Miller[4], Volker M. Nock[1,5], F. Grant Pearce[1,3] and Renwick C.J. Dobson[1,3*]

*Address all correspondence to: renwick.dobson@canterbury.ac.nz

1 Biomolecular Interaction Centre, University of Canterbury, Christchurch, New Zealand

2 Australian Synchrotron, Melbourne, Victoria, Australia

3 School of Biological Sciences, University of Canterbury, Christchurch, New Zealand

4 Protein Science & Engineering Team, Callaghan Innovation, Christchurch, New Zealand

5 Department of Electrical & Computer Engineering, University of Canterbury, Christchurch, New Zealand

References

[1] Bhatia, S.N. and D.E. Ingber, Microfluidic organs-on-chips. Nature Biotechnology, 2014. 32(8): p. 760–772.

[2] Whitesides, G.M., The origins and the future of microfluidics. Nature, 2006. 442(7101): p. 368–373.

[3] Hansen, C., Microfluidics in structural biology: smaller, faster… better. Current Opinion in Structural Biology, 2003. 13(5): p. 538–544.

[4] Pearce, F.G., et al., Characterization of monomeric dihydrodipicolinate synthase variant reveals the importance of substrate binding in optimizing oligomerization. Biochimica et Biophysica Acta, 2011. 1814(12): p. 1900–1909.

[5] Keown, J.R., et al., Small oligomers of ribulose-bisphosphate carboxylase/oxygenase (rubisco) activase are required for biological activity. Journal of Biological Chemistry, 2013. 288(28): p. 20607–20615.

[6] Cross, P.J., et al., Tyrosine latching of a regulatory gate affords allosteric control of aromatic amino acid biosynthesis. The Journal of Biological Chemistry, 2011. 286(12): p. 10216–10224.

[7] Mills, R.D., et al., Domain organization of the monomeric form of the tom70 mitochondrial import receptor. Journal of Molecular Biology, 2009. 388(5): p. 1043–1058.

[8] Griffin, M.D., et al., Characterisation of the first enzymes committed to lysine biosynthesis in Arabidopsis thaliana. PLoS One, 2012. 7(7): p. e40318.

[9] Crowther, J.M., et al., Ultra-high resolution crystal structure of recombinant caprine beta-lactoglobulin. FEBS Letters, 2014. 588(21): p. 3816–3822.

[10] Poen, S., et al., Exploring the structure of glutamate racemase from Mycobacterium tuberculosis as a template for anti-mycobacterial drug discovery. Biochemical Journal, 2016. 473(9): p. 1267–1280.

[11] Chen, K., et al., Genome-wide binding and mechanistic analyses of smchd1-mediated epigenetic regulation. Proceedings of the National Academy of Sciences of the United States of America, 2015. 112(27): p. E3535–E3544.

[12] Stehle, R., et al., Small-angle X-ray scattering in droplet-based microfluidics. Lab on a Chip, 2013. 13(8): p. 1529–1537.

[13] Panine, P., et al., Probing fast kinetics in complex fluids by combined rapid mixing and small-angle X-ray scattering. Advances in Colloid and Interface Science 2006. 127(1): p. 9–18.

[14] Hansen, C.L., et al., A robust and scalable microfluidic metering method that allows protein crystal growth by free interface diffusion. Proceedings of the National Academy of Sciences of the United States of America, 2002. 99(26): p. 16531–16536.

[15] Brennich, M.E., et al., Dynamics of intermediate filament assembly followed in micro-flow by small angle X-ray scattering. Lab on a Chip, 2011. 11(4): p. 708–716.

[16] Martel, A., et al., Silk fiber assembly studied by synchrotron radiation SAXS/WAXS and Raman spectroscopy. Journal of the American Chemical Society, 2008. 130(50): p. 17070–17074.

[17] Polte, J., et al., Nucleation and growth of gold nanoparticles studied via in situ small angle X-ray scattering at millisecond time resolution. ACS Nano, 2010. 4(2): p. 1076–1082.

[18] Otten, A., et al., Microfluidics of soft matter investigated by small-angle X-ray scattering. Journal of Synchrotron Radiation, 2005. 12(Pt 6): p. 745–750.

[19] Dootz, R., et al., Rapid prototyping of X-ray microdiffraction compatible continuous microflow foils. Small, 2007. 3(1): p. 96–100.

[20] Barrett, R., et al., X-ray microfocussing combined with microfluidics for on-chip X-ray scattering measurements. Lab on a Chip, 2006. 6(4): p. 494–499.

[21] Pollack, L., et al., Compactness of the denatured state of a fast-folding protein measured by submillisecond small-angle x-ray scattering. Proceedings of the National Academy of Sciences of the United States of America, 1999. 96(18): p. 10115–10117.

[22] Pollack, L., et al., Time resolved collapse of a folding protein observed with small angle x-ray scattering. Physical Review Letters, 2001. 86(21): p. 4962–4965.

[23] Akiyama, S., et al., Conformational landscape of cytochrome c folding studied by microsecond-resolved small-angle x-ray scattering. Proceedings of the National Academy of Sciences of the United States of America, 2002. 99(3): p. 1329–1334.

[24] Uzawa, T., et al., Collapse and search dynamics of apomyoglobin folding revealed by submillisecond observations of alpha-helical content and compactness. Proceedings of the National Academy of Sciences of the United States of America, 2004. 101(5): p. 1171–1176.

[25] Uzawa, T., et al., Time-resolved small-angle X-ray scattering investigation of the folding dynamics of heme oxygenase: implication of the scaling relationship for the submillisecond intermediates of protein folding. Journal of Molecular Biology, 2006. 357(3): p. 997–1008.

[26] Kimura, T., et al., Specific collapse followed by slow hydrogen-bond formation of beta-sheet in the folding of single-chain monellin. Proceedings of the National Academy of Sciences of the United States of America, 2005. 102(8): p. 2748–2753.

[27] Graceffa, R., et al., Sub-millisecond time-resolved SAXS using a continuous-flow mixer and X-ray microbeam. Journal of Synchrotron Radiation, 2013. 20(Pt 6): p. 820–825.

[28] Arai, M., et al., Microsecond hydrophobic collapse in the folding of Escherichia coli dihydrofolate reductase, an alpha/beta-type protein. Journal of Molecular Biology, 2007. 368(1): p. 219–229.

[29] Wu, Y., et al., Microsecond acquisition of heterogeneous structure in the folding of a TIM barrel protein. Proceedings of the National Academy of Sciences of the United States of America, 2008. 105(36): p. 13367–13372.

[30] Russell, R., et al., Rapid compaction during RNA folding. Proceedings of the National Academy of Sciences of the United States of America, 2002. 99(7): p. 4266–4271.

[31] Kimura, T., et al., Specifically collapsed intermediate in the early stage of the folding of ribonuclease A. Journal of Molecular Biology, 2005. 350(2): p. 349–-362.

[32] Toft, K.N., et al., High-throughput small angle X-ray scattering from proteins in solution using a microfluidic front-end. Analytical Chemistry, 2008. 80(10): p. 3648–3654.

[33] Lafleur, J.P., et al., Automated microfluidic sample-preparation platform for high-throughput structural investigation of proteins by small-angle X-ray scattering. Journal of Applied Crystallography, 2011. 44(5): p. 1090–1099.

[34] Schwemmer, F., et al., LabDisk for SAXS: a centrifugal microfluidic sample preparation platform for small-angle X-ray scattering. Lab on a Chip, 2016. 16(7): p. 1161–1170.

[35] Round, A.R., et al., Automated sample-changing robot for solution scattering experiments at the EMBL hamburg SAXS station X33. Journal of Applied Crystallography, 2008. 41(Pt 5): p. 913–917.

[36] Greaves, E.D. and A. Manz, Toward on-chip X-ray analysis. Lab on a Chip, 2005. 5(4): p. 382–391.

[37] Moller, M., et al., Small angle X-ray scattering studies of mitochondrial glutaminase C reveal extended flexible regions, and link oligomeric state with enzyme activity. PLoS One, 2013. 8(9): p. e74783.

[38] Skou, M., et al., In situ microfluidic dialysis for biological small-angle X-ray scattering. Journal of Applied Crystallography, 2014. 47(4): p. 1355–1366.

[39] Kihara, H., Stopped-flow apparatus for X-ray scattering and XAFS. Journal of Synchrotron Radiation, 1994. 1(Pt 1): p. 74–77.

[40] Eliezer, D., et al., The radius of gyration of an apomyoglobin folding intermediate. Science, 1995. 270(5235): p. 487–488.

[41] Arai, M., et al., Kinetic refolding of β-lactoglobulin. Studies by synchrotron X-ray scattering, and circular dichroism, absorption and fluorescence spectroscopy1. Journal of Molecular Biology, 1998. 275(1): p. 149–162.

[42] Plaxco, K.W., et al., Chain collapse can occur concomitantly with the rate-limiting step in protein folding. Nature Structural Biology, 1999. 6(6): p. 554–556.

[43] Jacob, J., et al., Early collapse is not an obligate step in protein folding. Journal of Molecular Biology, 2004. 338(2): p. 369–382.

[44] Tsuruta, H., et al., Influence of nucleotide effectors on the kinetics of the quaternary structure transition of allosteric aspartate transcarbamylase. Journal of Molecular Biology, 2005. 348(1): p. 195–204.

[45] Roh, J.H., et al., Multistage collapse of a bacterial ribozyme observed by time-resolved small-angle X-ray scattering. Journal of the American Chemical Society, 2010. 132(29): p. 10148–10154.

[46] Moody, M.F., et al., Stopped-flow x-ray scattering: the dissociation of aspartate transcarbamylase. Proceedings of the National Academy of Sciences of the United States of America, 1980. 77(7): p. 4040–4043.

[47] Regenfuss, P., et al., Mixing liquids in microseconds. Review of Scientific Instruments, 1985. 56(2): p. 283.

[48] Moskowitz, G.W. and R.L. Bowman, Multicapillary mixer of solutions. Science, 1966. 153(3734): p. 428–429.

[49] Chan, C.K., et al., Submillisecond protein folding kinetics studied by ultrarapid mixing. Proceedings of the National Academy of Sciences of the United States of America, 1997. 94(5): p. 1779–1784.

[50] Segel, D.J., et al., Characterization of transient intermediates in lysozyme folding with time-resolved small-angle X-ray scattering. Journal of Molecular Biology, 1999. 288(3): p. 489–499.

[51] Takahashi, S., et al., Folding of cytochrome c initiated by submillisecond mixing. Nature Structural Biology, 1997. 4(1): p. 44–50.

[52] Bilsel, O., et al., A microchannel solution mixer for studying microsecond protein folding reactions. Review of Scientific Instruments, 2005. 76(1): p. 014302.

[53] Knight, J.B., et al., Hydrodynamic focusing on a silicon chip: mixing nanoliters in microseconds. Physical Review Letters, 1998. 80(17): p. 3863–3866.

[54] Park, H.Y., et al., Conformational changes of calmodulin upon Ca^{2+} binding studied with a microfluidic mixer. Proceedings of the National Academy of Sciences of the United States of America, 2008. 105(2): p. 542–547.

[55] Hertzog, D.E., et al., Femtomole mixer for microsecond kinetic studies of protein folding. Analytical Chemistry, 2004. 76(24): p. 7169–7178.

Chapter 5

SAXS Evaluation of Size Distribution for Nanoparticles

Shinichi Sakurai

Additional information is available at the end of the chapter

http://dx.doi.org/10.5772/105981

Abstract

Size distribution is an important structural aspect in order to rationalize relationship between structure and property of materials utilizing polydisperse nanoparticles. One may come to mind the use of dynamic light scattering (DLS) for the characterization of the size distribution of particles. However, only solution samples can be analyzed and even for those, the solution should be transparent or translucent because of using visible light. It is needless to say that solid samples are out of range. Furthermore, the size distribution only in the range of several tens of nanometers can be characterized, so DLS is useless for particles in the range of several nanometers. Therefore, the small-angle X-ray scattering (SAXS) technique is much superior when considering the determination of the size distribution in several nanometers length scale for opaque solutions and for solid specimens. Furthermore, the SAXS technique is applicable not only for the spherical particle but also for platelet (lamellar) and rod-like (cylindrical) particles. In this chapter, we focus on the form factor of a variety of nanostructures (spheres, prolates, core-shell spheres, core-shell cylinders and lamellae). Also getting started with a monodisperse distribution of the size of the nanostructure, to unimodal distribution with a narrow standard deviation or wide-spreading distribution and finally to the discrete distribution can be evaluated by the computational parameter fitting to the experimentally obtained SAXS profile. In particular, for systems forming complicated aggregations, this methodology is useful. Not only the size distribution of 'a bunch of grapes' but also the size distribution of all 'grains of grapes in the bunch' can be evaluated according to this methodology. This is very much contrasted to the case of the DLS technique by which only 'a bunch of grapes' is analyzed but 'grains of grapes in the bunch' cannot be. It is because the DLS technique in principle evaluates diffusion constants of particles and all of the grains in the same bunch of grapes diffuse as a whole. Thus, the methodology is important to highlight versatility and diversity in real materials, especially in soft matter, both in the liquid and in the solid states.

Keywords: SAXS, form factor, sphere, cylinder, lamella, prolate, core-shell sphere, core-shell cylinder, discrete distribution function

1. Introduction

In recent years, controlling of nanostructures has been more significantly considered in the field of materials science, especially relating to the soft matter [1]. Versatile properties or functions can be obtained through designing nanostructures in solid-state materials, as well as nanomaterials dispersed in liquid-state substance. Even for contradictory properties such as hard and soft, they may be coexistent in one material when fabricating so-called inclined nanostructures (for instance, nanoparticle size is gradually changing as a function of the position in material). This in turn indicates that size distribution of the nanostructures should be rigorously evaluated for better understanding effects of nanostructure on properties and functions. For biological systems or supramolecular organizations, situation is very much contrast to the other ubiquitous materials as described above because they form spontaneously a regular aggregation. Therefore, the size distribution is narrow and follows a simple mathematical function with a comparatively small standard deviation. By contrast, discrete distribution of the size is required to determine for the ubiquitous materials. However, even for regular nanostructures, the determination of the discrete distribution of the nanostructure size is needed to reveal a transient state upon transition from the state 1 to the state 2, being triggered by sudden change in temperature, pH, or other external parameters.

It is well known that the size distribution of particles can be evaluated by the use of dynamic light scattering (DLS). However, only solution samples can be analyzed and even for those, the solution should be transparent or translucent because of using visible light. It is needless to say that solid samples are out of range. Furthermore, the size distribution only in the range of several tens of nanometers can be characterized, so DLS is useless for particles in the range of several nanometers. Therefore, the small-angle X-ray scattering (SAXS) technique is much superior when considering the determination of the size distribution in several nanometers length scale for opaque solutions and for solid specimens [2]. Furthermore, the SAXS technique is applicable, not only for the spherical particle but also for platelet (lamellar) and rod-like (cylindrical) particles and it enables us to determine the thickness distribution of lamellae or the cross-sectional radius distribution of cylinders. Namely, the SAXS technique does not matter types of particle shape even for hallow cylinders or hollow spheres [3].

The principle is simple. Scattering comprises not only contribution from regularity of space-filling ordering (the lattice factor) of particles but also from a single particle (the form factor). The particle scattering can be mathematically formulated depending on the type of particle shape (lamella, cylinder or sphere). In the block copolymer microdomain systems, the Gauss distribution of the particle size has been assumed. Only recently, direct determination of the discrete size distribution has been available by conducting fitting theoretical scattering function to the experimentally obtained SAXS profile (the plot of the scattering intensity as a function of the magnitude of the scattering vector, q [= $(4\pi/\lambda)$ sin $(\Theta/2)$ with Θ and λ being the scattering angle and the wavelength of X-ray, respectively] where the abundance of the particle having a given size was treated as a floating parameter with a step of 1 nm (the step can be more precise). In this chapter, getting started

with nanoparticles with a narrow size distribution, we will see characteristic shape of the form factors for protein self-assembly, block copolymer microdomains and peptide amphiphile nanofibers. Then, we shift our target to the evaluation of discrete distribution of size of nanostructures by SAXS. The examples shown are thickness distribution of the crystalline lamellae of polyethylene glycol in polymer blends and thickness distribution of the hard segment domains for supramolecular elastomers (starblocks of soft polyisobutylene and hard oligo(β-alanine) segments). Other notable examples are sterically stabilized polypyrrole-palladium (PPy-Pd) nanocomposite particles, hybrid amphiphilic poly(N-isopropylacrylamide)/metal cyanide complexes and the cobalt(II) terpyridine complexes with diblock copolypeptide amphiphiles. For this example, this methodology is useful. Not only the size distribution of 'a bunch of grapes' but also the size distribution of all 'grains of grapes in the bunch' can be evaluated according to this methodology. This is very much contrasted to the case of the DLS technique by which only 'a bunch of grapes' is analyzed but 'grains of grapes in the bunch' cannot be. It is because the DLS technique in principle evaluates diffusion constants of particles and all of the grains in the same bunch of grapes diffuse as a whole. Thus, the methodology is important to highlight versatility and diversity in real materials, especially in soft matter, both in the liquid and in the solid states.

2. Nanoparticles with a narrow size distribution

First of all, some typical examples of the experimentally observed form factor are demonstrated. The samples are self-assembly of proteins, block copolymer microdomains and peptide amphiphiles. Apoferritin is a protein having ability to store iron atoms and it is referred to as ferritin when iron atoms are bound. Apoferritin forms a spherical shell as a self-assembled nanostructure with a very uniform size. As indicated in **Figure 1** (pH-dependence of SAXS profiles), its SAXS profiles (apoferritin, 24-mer) exhibit characteristic features with many peaks due to its uniform shape for pH ≥3.40 [4]. Dramatic change in the SAXS profile is detected between pH = 1.90 and 3.40. This means that apoferritin is disassembled for acidic condition. Time-resolved SAXS measurements have been utilized to study disassembling and reassembling process upon the change in pH [4, 5]. In **Figure 1**, the curve shows the result of the SAXS modeling by the scattering program GNOM [6]. Since protein molecules produce the typical form factor, it is frequently used to obtain commissioning data for newly launched SAXS beamline or apparatus [7–9].

It is known that block copolymer spontaneously forms a regular nanostructure with a narrow size distribution. **Figure 2** shows examples of the SAXS profiles for sphere-forming block copolymer (SEBS; polystyrene-block-poly(ethylene-co-butylene)-block-polystyrene triblock copolymer) having Mn = 6.7×10^4, Mw/Mn = 1.04, PS volume fraction = 0.084) [10], where Mn and Mw denote number-average and weight-average molecular weights, respectively. In **Figure 2**, the solid curve is the results of the model calculation for the spherical particle, but not only the form factor, but also the lattice factor of BCC (body-centered cubic) is taken into account. The full equation is as follows [11–14]:

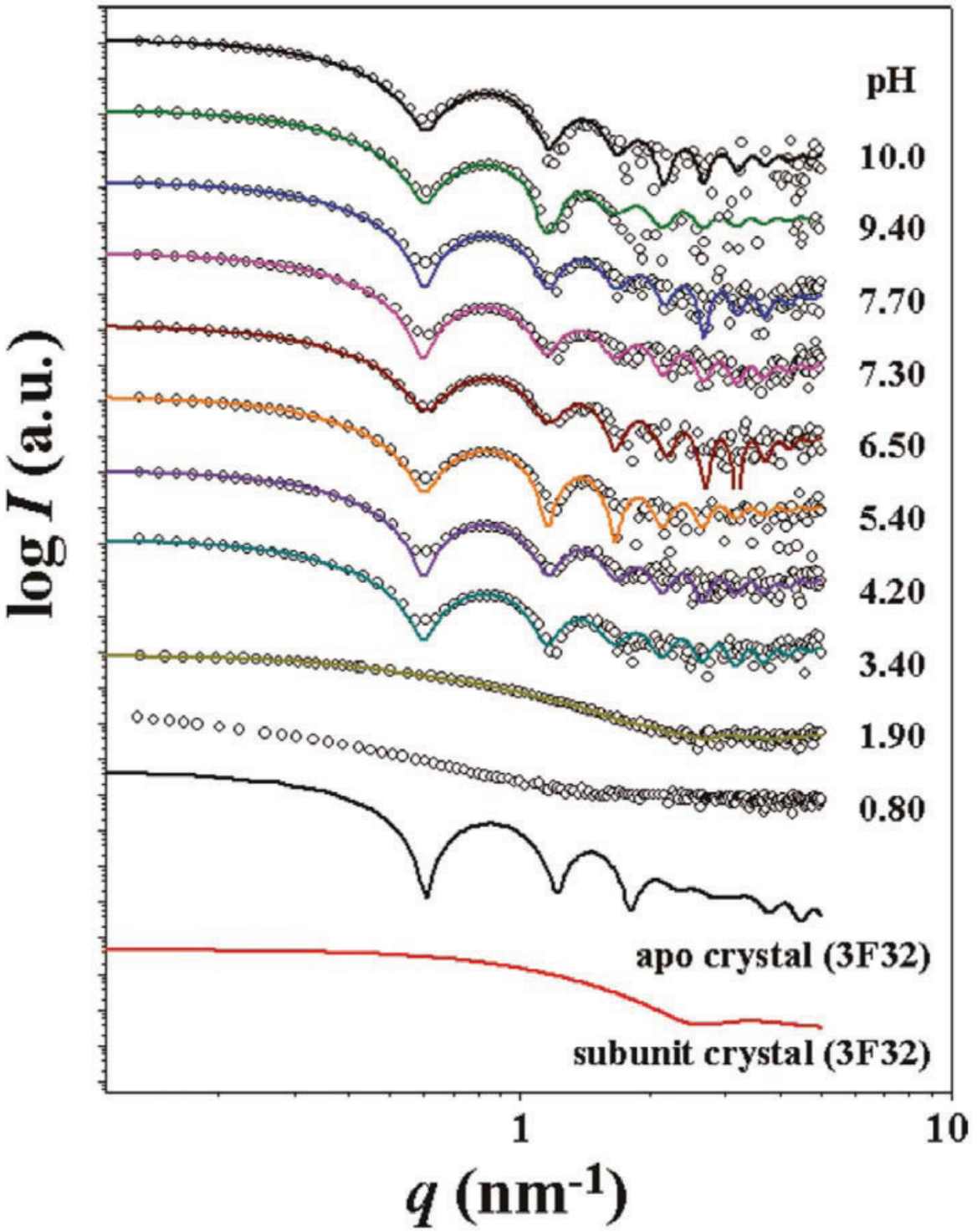

Figure 1. pH-dependence of SAXS profiles for an apoferritin aqueous solution. The symbols indicate the experimental data, and the solid lines indicate the fits obtained using the GNOM program. The solid lines without symbols are the theoretical SAXS curves calculated from the crystal structure of apoferritin and its subunit crystal (PDB code 3F32). For clarity, each plot is shifted along the log I axis [4].

http://dx.doi.org/10.5772/105981

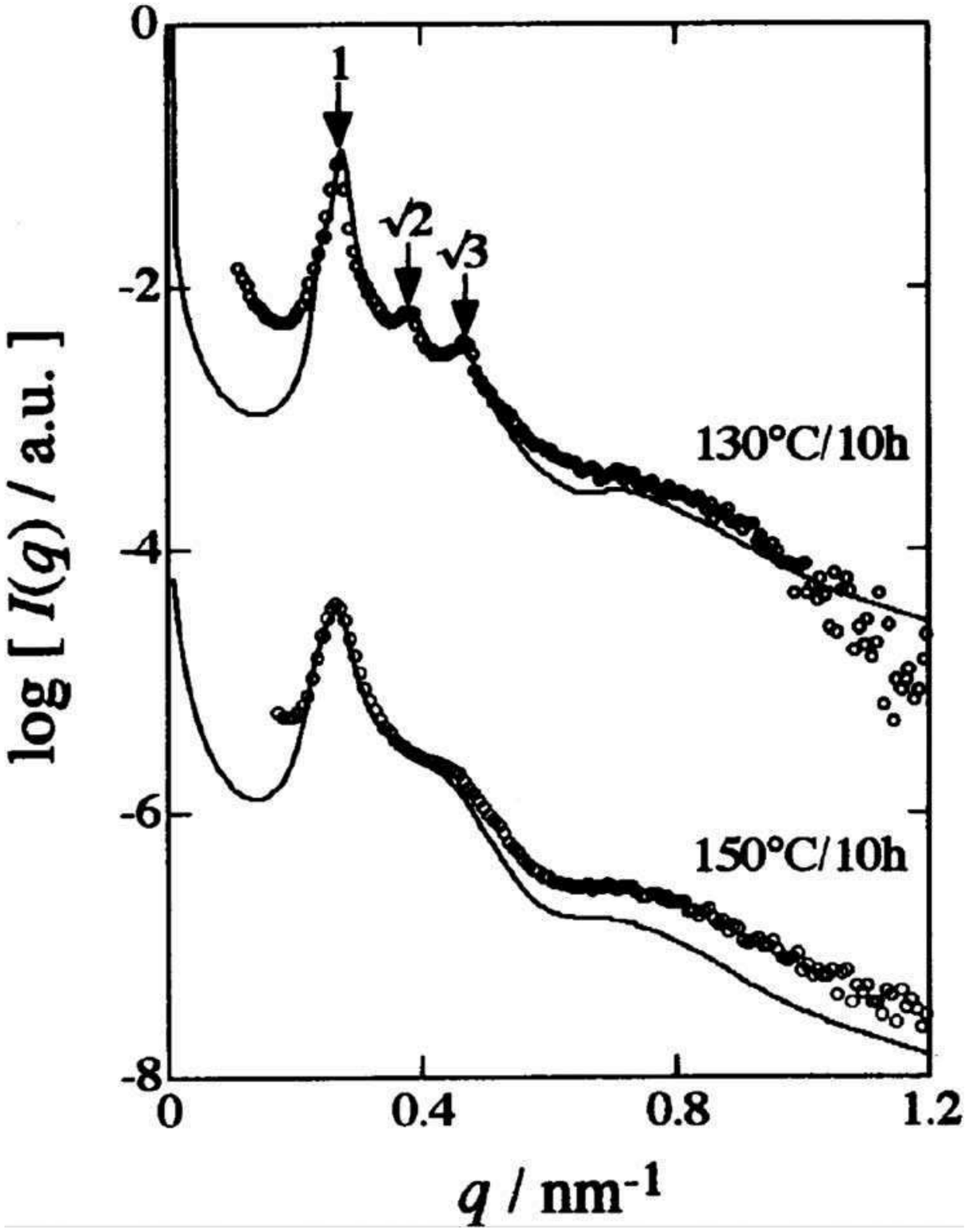

Figure 2. SAXS profiles for SEBS-8 specimens (sphere-forming triblock copolymer) annealed at 130 and 150°C for 10 h [10].

$$I(q) - \langle |f^2(q)| \rangle - |\langle f(q) \rangle|^2 + |\langle f(q) \rangle|^2 Z(q) \tag{1}$$

where <x> is the average of the quantity of x. $f(q)$ and $Z(q)$ are particle and lattice factor, respectively, designating the scattering amplitude due to the intraparticle interference and the scattering intensity due to the interparticle interference, respectively. The form factor $f(q)$ for a spherical particle with its radius, R, can be given as

$$f(q) = A_e \Delta\rho \, V \frac{3[\sin(qR) - qR\cos(qR)]}{(qR)^3} \tag{2}$$

where A_e is the scattering amplitude of the Thomson scattering, $\Delta\rho$ is the difference in the electron density between sphere and matrix, V is the volume of the spheres. Here, the Gauss distribution is used for R with σ_R being the standard deviation. On the other hand, the lattice factor $Z(q)$ is given by Eq. (3) with Eulerian angles, θ and ϕ, which define orientation of the unit cell of a given grain with respect to the experimental Cartesian coordinates:

$$\begin{aligned} Z(q,\theta,\phi) = & \frac{1 - F_k^2}{\left[1 - 2F_k \cos\left(\frac{\sqrt{6}}{4} qd\alpha\right) + F_k^2\right]} \\ & \times \frac{1 - F_k^2}{\left[1 - 2F_k \cos\left(\frac{\sqrt{6}}{4} qd\beta\right) + F_k^2\right]} \times \frac{1 - F_k^2}{\left[1 - 2F_k \cos\left(\frac{\sqrt{6}}{4} qd\gamma\right) + F_k^2\right]} \end{aligned} \tag{3}$$

with

$$F_k = \exp\left[-\frac{3}{16} g^2 d^2 q^2 (\alpha^2 + \beta^2 + \gamma^2)\right] \tag{4}$$

and $g = \Delta d / \langle d \rangle$ which is the degree of the lattice distortion (Δd denotes the standard deviation in d due to the paracrystalline distortion). In Eq. (4),

$$\alpha = \sin\theta\cos\phi + \sin\theta\sin\phi + \cos\theta \tag{5}$$

$$\beta = -\sin\theta\cos\phi - \sin\theta\sin\phi + \cos\theta \tag{6}$$

$$\gamma = -\sin\theta\cos\phi + \sin\theta\sin\phi - \cos\theta \tag{7}$$

for the bcc lattice and

$$\alpha = \sin\theta\sin\phi + \cos\theta \tag{8}$$

$$\beta = -\sin\theta\cos\phi + \cos\theta \tag{9}$$

$$\gamma = -\sin\theta\cos\phi + \sin\theta\sin\phi \tag{10}$$

for the fcc lattice. In Eqs. (3) and (4), d denotes the Bragg spacing. The spacing for {110} and {111} planes for the bcc and fcc lattices, respectively, gives rise to the first-order peaks. For

randomly oriented polygrains in actual samples, the scattering is isotropic. Therefore, $Z(q,\theta,\phi)$ is averaged with respect to θ and ϕ to obtain isotropic $Z(q)$:

$$Z(q) = \frac{1}{4\pi}\int_0^{2\pi}\int_0^{\pi} Z(q,\theta,\phi)\sin\theta d\theta d\phi \tag{11}$$

As clearly observed in **Figure 2**, the broad peak around q = 0.71 nm^{-1} is due to the form factor. The model curve is the result of calculation with <*R*> = 7.90 nm for 130°C annealed specimen and <*R*> = 8.10 nm for 150°C annealed specimen and the standard deviation of the size distribution (σ_R) being 1.09 and 1.10 nm, respectively. Thus, evaluated value of <*R*> is consistent with the result of transmission electron microscopic observation (as shown in **Figure 3**). Note also here that the order-disorder transition temperature locates between 130 and 150°C, so that bcc ordering is quite regular for the specimen annealed at 130°C, while it is poor for 150°C annealed specimen. The SAXS profile for the 130°C annealed specimen displays clear lattice peaks at the relative q values of 1:√2:√3, indicating high regularity of the bcc ordering. The sphere-forming block copolymers exhibit mostly the bcc ordering due to the entropic profit [14] and the fcc ordering has been found for some particular case. Comparison between the results shown in **Figures 1** and **2** clearly indicates that many peaks for monodisperse particle are easy to collapse to become more featureless when the size distribution is incorporated even if it is small. Nevertheless, it is characteristic for the block copolymer microdomains that one peak can be discernible for the form factor.

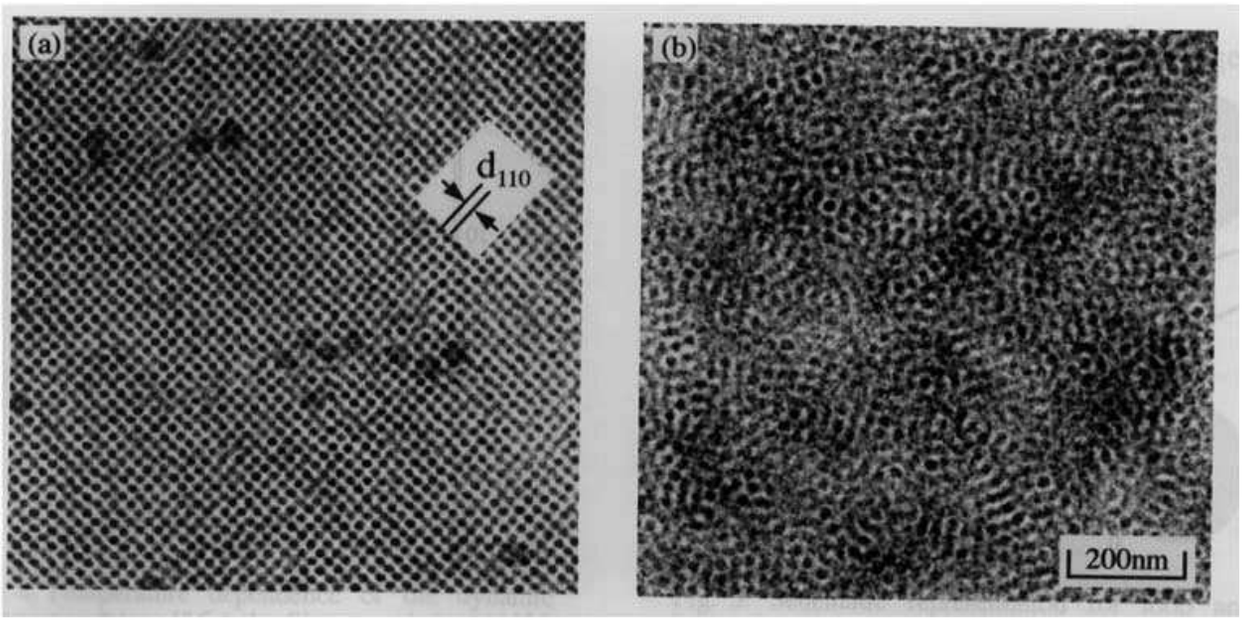

Figure 3. TEM micrographs for SEBS-8 specimens annealed at (a) 130 and (b) 150°C for 10 h. The polystyrene microdomains were stained with ruthenium tetroxide [10].

Very recently, it has been found that PS spherical microdomains were deformed upon the uniaxial stretching of the SEBS-8 film specimens [15]. Since SEBS triblock copolymer with the glassy PS spherical microdomains can be used as a thermoplastic elastomer (TPE), the film

specimen can be stretched. In **Figure 4**, 2D-SAXS patterns are displayed to recognize the deformation of the round shape form factor upon the uniaxial stretching. **Figure 4a** shows the 2D-SAXS pattern for the SEBS-8 film specimen. Here, it is clearly observed that the round shape form factor appears at q = 0.77 nm^{-1}. The round peak of the form factor is deformed to become an ellipsoid in **Figure 4b** upon uniaxial stretching of the film specimen up to the strain of 3.65 (stretching ratio is 4.65) at room temperature. The peak position in the $\boldsymbol{q}^{-}$direction parallel to the stretching direction ($\boldsymbol{q}$//SD) is lower than that in the $\boldsymbol{q}^{-}$direction perpendicular to SD ($\boldsymbol{q}\perp$SD). This means that the size of the particle in the $\boldsymbol{q}_{//}$ direction is bigger than that in $\boldsymbol{q}_{\perp}$ direction, which in turn implies deformation of the spherical particles. Therefore, the model calculation of the form factor, $P(q)$, for prolate was conducted using the mathematical equation as follows:

$$P(q) = \int_0^{2\pi} \int_0^{\pi/2} \int_0^{\infty} \int_1^{\infty} f^2(q, v, R_{\min}, \phi)\ \Omega(v)\ \Xi(R_{\min})\ \Psi_{\phi}(\phi)\Psi_{\mu}(\mu) \sin\phi\ dv\ dR_{\min}\ d\phi d\mu \tag{12}$$

$$f(q, v, R_{\min}) = V\frac{3(\sin U - U\cos U)}{U^3} \tag{13}$$

$$U(q, v, R_{\min}, \phi) = qR_{\min}\sqrt{\sin^2\phi + v^2\cos^2\phi} \quad for\ q//SD \tag{14}$$

$$U(q, v, R_{\min}, \phi, \mu) = qR_{\min}\sqrt{\sqrt{1-\sin^2\phi\cos^2\mu} + v^2\sin^2\phi\cos^2\mu} \quad \text{for } q\perp\text{SD} \tag{15}$$

$$v = \frac{R_{\text{maj}}}{R_{\min}} > 1 \qquad V = \frac{4\pi}{3}R_{maj}R_{\min}^2 = \frac{4\pi}{3}vR_{\min}^3 \quad \text{and (volume of the prolate)} \tag{16}$$

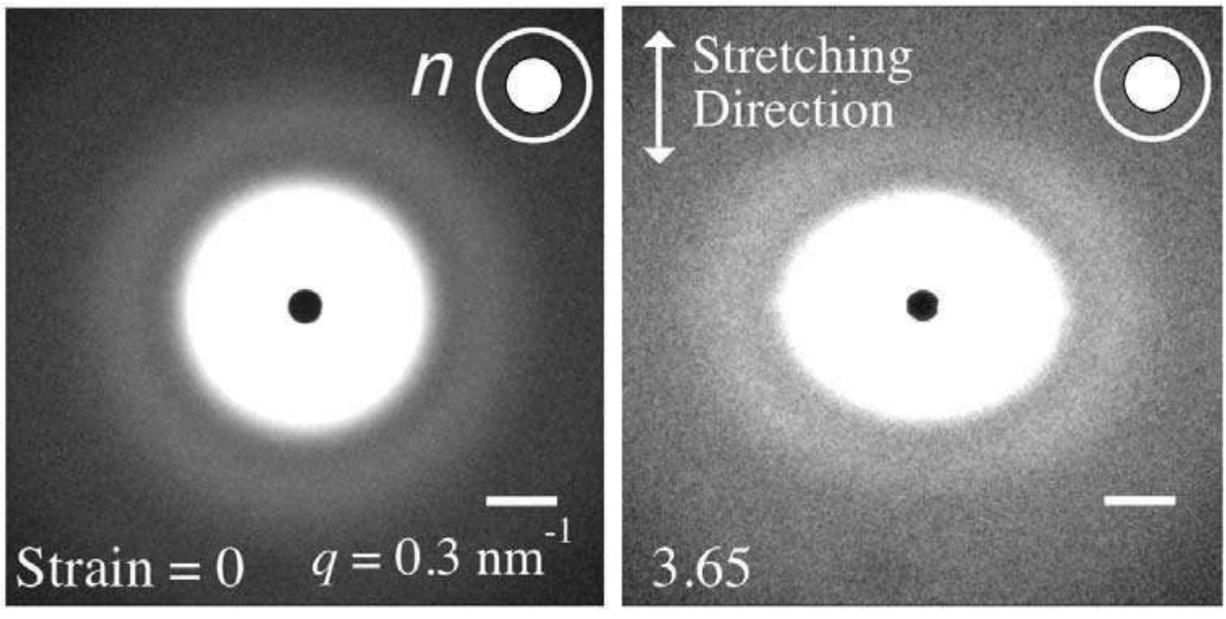

Figure 4. 2D-SAXS patterns for SEBS-8 specimens (a) unstretched state and (b) being stretched at the strain of 3.65 at room temperature [15].

Here, R_{maj} and R_{min} stand for the radius of the longer axis and the radius of the shorter axis of the prolate, respectively (**Figure 5**) and ϕ is the angle between the $\boldsymbol{q}$ direction and the long axis of the prolate. To fit the SAXS profile with the model calculation, the distributions in R_{min}, ν and ϕ are required. Note here that the distributions in ϕ and μ define the orientational distribution function: $\Psi_{\phi}(\phi)$ and $\Psi_{\mu}(\mu)$, respectively. However, for this particular case, ϕ can be considered to be zero with no distribution, namely perfect orientation of the prolates with their log axes parallel to SD because the uniaxial stretching prolongs spherical microdomains to result in prolates with their long axes parallel to SD, which in turn enables us to set $\Psi_{\mu}(\mu) = 1$ regardless of μ. Therefore, due to decreased numbers of the parameters, the situation became easier to evaluate the average values of R_{min} and ν with their distributions (ΞR_{min} and $\Omega(\nu)$).

The results for the 1D-SAXS profiles in $\boldsymbol{q}_{//}$ and in $\boldsymbol{q}_{\perp}$ directions are shown in **Figure 6a** and **b**, respectively. In the both cases, the 1D-SAXS profile for the unstretched film specimen (before the stretching) is shown together. It is clearly observed that the peak of the form factor moved toward lower and higher q range upon the stretching in $\boldsymbol{q}_{//}$ and in $\boldsymbol{q}_{\perp}$ directions, respectively. Furthermore, both of the SAXS profiles can be fit by the prolate model, using Eqs. (1), (12)–(16) with the bcc lattice factor. Here, the $<R_{min}>$ = 6.44 nm and $<\nu>$ = 1.20 were used for the model calculation. Note that $<R_{min}>$ = 6.85 nm for the unstretched specimen. Moreover, the distributions in R_{min} and ν (ΞR_{min} and $\Omega(\nu)$) used for the calculation are plotted in **Figure 7a** and **b**, respectively. Such a mathematical function for the size distribution is enough to explain the experimentally observed SAXS profile under the stretched state. However, it should be noted that both of the distributions were required and otherwise, the model SAXS curve did not fit well the experimental results for both the $\boldsymbol{q}_{//}$ and $\boldsymbol{q}_{\perp}$ directions. **Figure 6a** and **b** also includes the SAXS profiles measured after complete removal of the stretching force. At a first glance, the peak positions of the form factor in **Figure 6a** and **b** seem to recover its original position for the unstretched specimens. However, this does not imply the recovery of the original spherical shape upon the removal of the load because the deformation of the glassy PS microdomains is permanent. Then, why did the form factor recover its original peak position? It may be ascribed to randomization of the prolates orientation upon the removal of the load. To check this speculation, we conducted the SAXS modeling of the prolate form factor by setting $\Psi(\phi) = 1$ irrespective of ϕ but with keeping the size distribution R_{min} and ν (ΞR_{min} and $\Omega(\nu)$) unchanged. The results of the modeling are shown with the red curves in **Figure 6a** and **b**, indicating clearly good agreements with the experimentally obtained SAXS profiles. This in turn confirms the speculation of randomization of the prolates orientation upon the removal of the load.

Core-shell sphere and cylinder models are significantly important for the amphiphilic self-assembly. For the core-shell sphere [16, 17], the form factor is formulated as:

$$P(q) = \left\{ (\rho_C - \rho_S) V_C \frac{3[\sin(qR_C) - qR_C \cos(qR_C)]}{(qR_C)^3} + (\rho_S - \rho_0) V_S \frac{3[\sin(qR_S) - qR_S \cos(qR_S)]}{(qR_S)^3} \right\}^2 \quad (17)$$

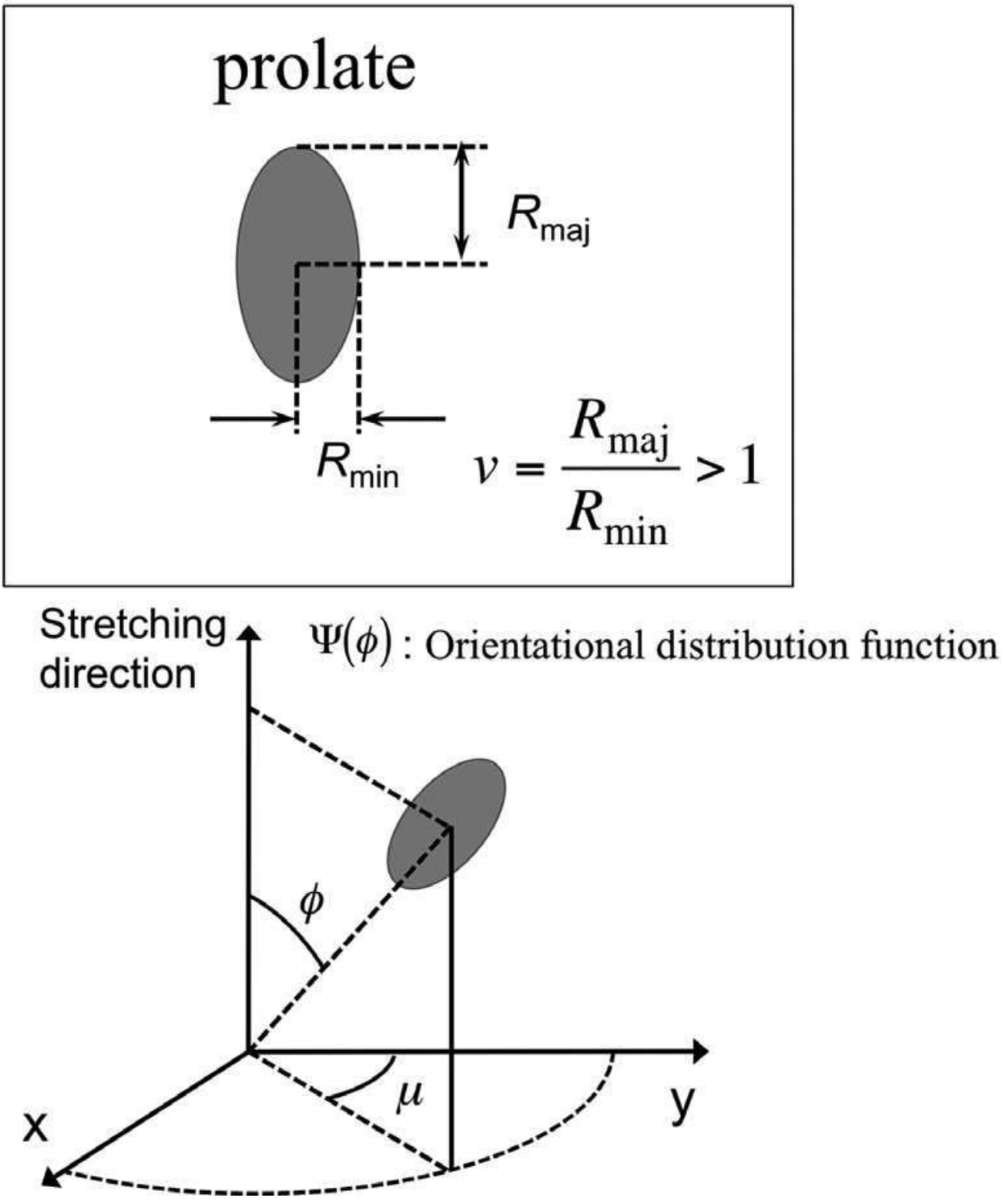

Figure 5. Prolate model used for the SAXS modeling. Here, R_{maj} and R_{min} stand for the radius of the longer axis and the radius of the shorter axes of the prolate, respectively. Eulerian angles, μ and ϕ, define orientation of the prolate with respect to the experimental Cartesian coordinates [15].

http://dx.doi.org/10.5772/105981

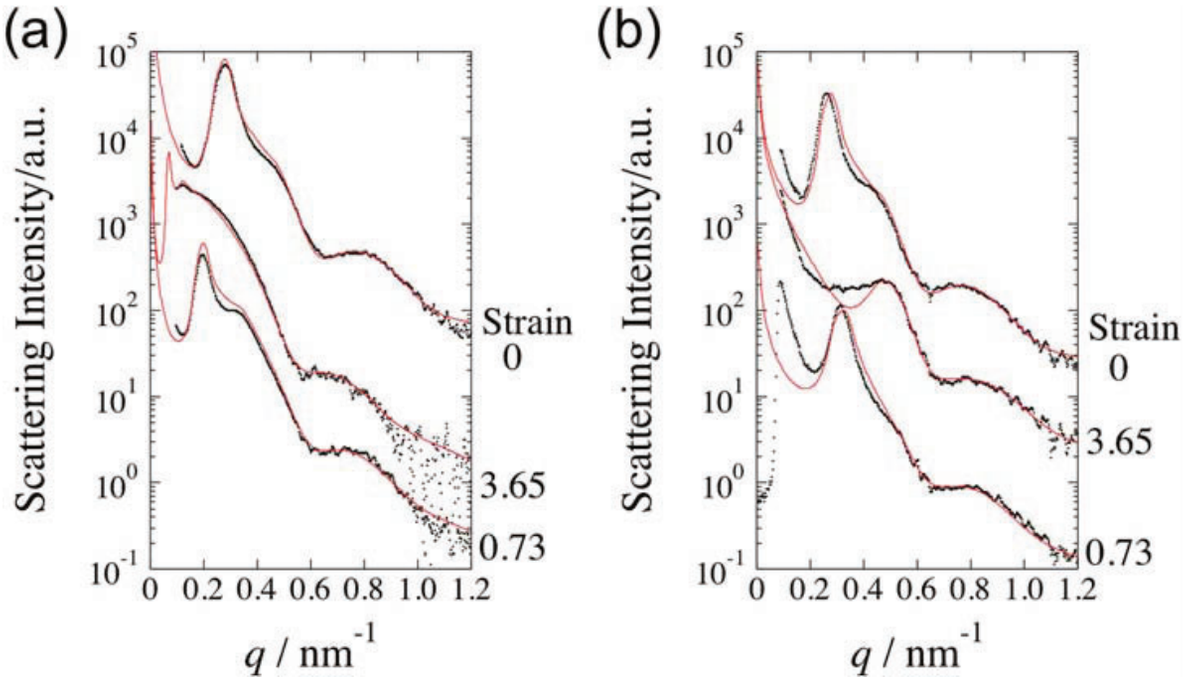

Figure 6. 1D-SAXS profiles extracted from the SAXS patterns as shown in **Figure 5** in (a) $q_{//}$ and in (b) $q_{\perp}$ directions. Black dots are for the experimentally obtained SAXS profiles, and red curves are calculated SAXS profiles [15].

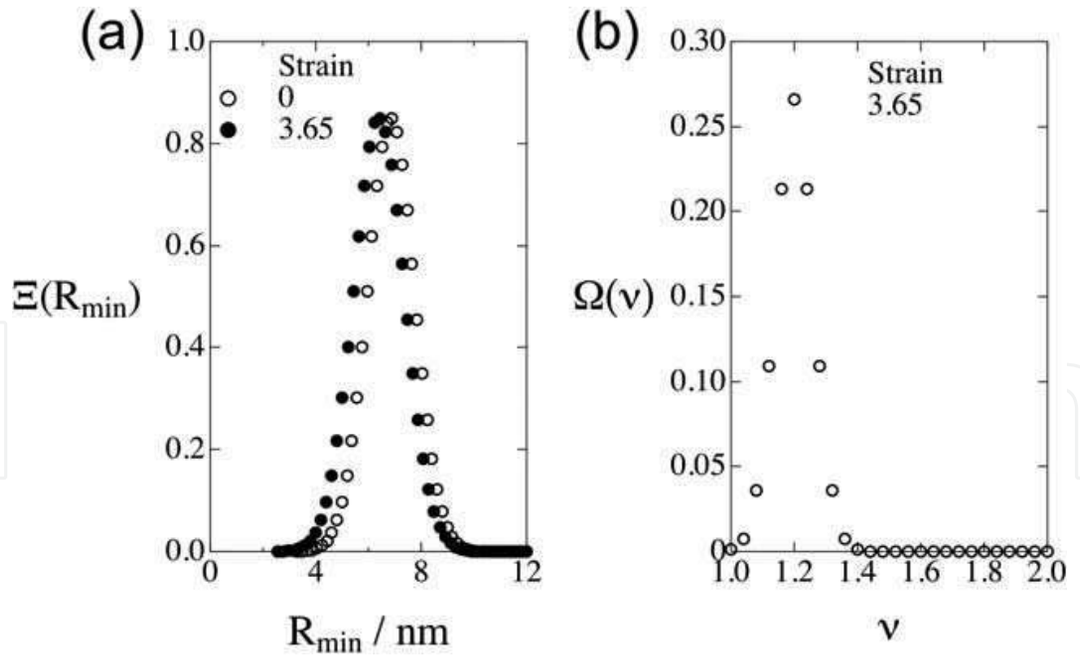

Figure 7. Evaluated $\Xi(R_{\min})$ and $\Omega(\nu)$ of the prolate for SEBS-8 specimens stretched at the strain of 3.65. For comparison, the size distribution function for the radius of sphere is shown together for the unstretched specimen [15].

if the homogeneous densities in the core and in the shell can be assumed with ρ_c and ρ_s, respectively. Here, V_c and V_s designate the volume of the core and the shell, respectively. Moreover, R_c and R_s denote the radii of the core and the shell, respectively. ρ_0 is the electron density of the matrix. On the other hand, when the shell density changes as a function of r (the core density is homogeneous) as defined with $\rho_s(r)$, then the form factor is formulated as [18, 19]:

$$P(q) = \left\{ (\rho_C - \rho_S) V_C \frac{3[\sin(qR_C) - qR_C \cos(qR_C)]}{(qR_C)^3} + 4\pi \int_{R_C}^{R_S} \left(\rho_S(r) - \rho_0\right) r^2 \frac{\sin(qr)}{qr} dr \right\}^2 \quad (18)$$

As for core-shell cylinders, the form factor is:

$$P(q) = \int_0^{\pi/2} \left\{ (\rho_S - \rho_{solv}) V_S \frac{\left[\sin\left(\frac{qH_S \cos\theta}{2}\right)\right]}{\frac{qH_S \cos\theta}{2}} \frac{2J_1(qR_S \sin\theta)}{qR_S \sin\theta} + \right.$$
$$\left. (\rho_C - \rho_S) V_C \frac{\left[\sin\left(\frac{qH_C \cos\theta}{2}\right)\right]}{\frac{qH_C \cos\theta}{2}} \frac{2J_1(qR_C \sin\theta)}{qR_C \sin\theta} \right\}^2 \sin\theta d\theta \quad (19)$$

where $J_1(x)$ is the first-order Bessel function. θ is defined as the angle between the cylinder axis and $\boldsymbol{q}$. R_C and R_S are the core and shell radii, respectively. H_C and H_S are the core and shell lengths, respectively. V_C and V_S are the core and shell volumes, respectively ($V_x = \pi R_x^2 H_x$; x = C, S, or $solv$; C: core, S: shell, $solv$: solvent). ρ_x is the electron density of the core, shell, or solvent.

Matson et al. [20] have reported the SAXS modeling of the form factor of the core-shell cylinder for self-assembling peptide amphiphiles (PAs) as shown in **Figure 8A** and **B**. The molecules self-assembled into the core-shell cylinder are illustrated in **Figure 8C**. Such cylinders can be detected with cryogenic TEM as shown in **Figure 9**. The SAXS profile is shown in **Figure 10** with the model curve, where the size distribution in the core radius is modeled using a log-normal distribution with the polydispersity being around 27–30% (see **Table 1** for the structural parameter determined by the SAXS modeling), while the radial shell thickness is assumed to be monodisperse. Although the modeling results explain very well the experimentally obtained SAXS profiles, the fact that the radial shell thickness is assumed to be monodisperse means it is difficult to determine individually two distributions in inner and outer radius. For more detailed structure analyses, more experimental variations are required to gather information from different kinds of aspects, like the example shown in **Figure 6a** and **b** (parallel and perpendicular to SD).

http://dx.doi.org/10.5772/105981

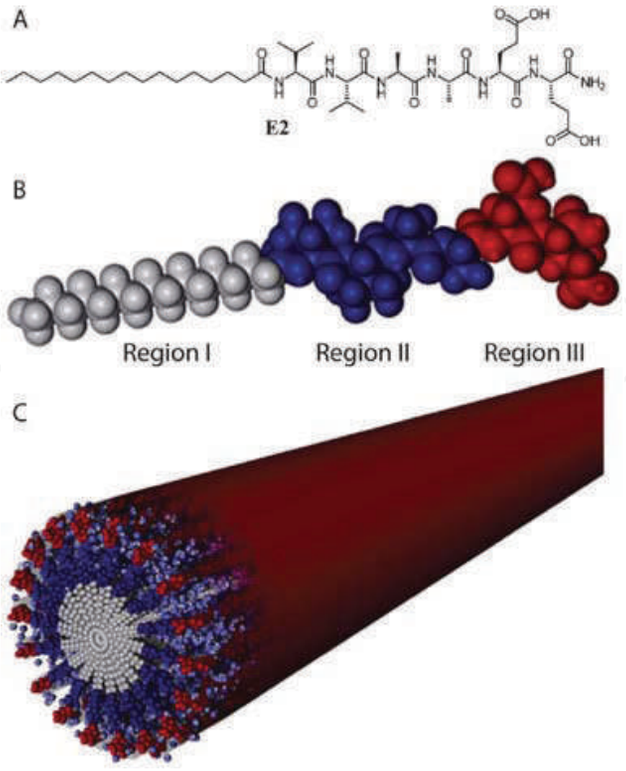

Figure 8. (A) Chemical structure of self-assembling peptide amphiphiles (PA: E2 C16V2A2E2). (B) The different regions of the PA are highlighted in a space-filling model. (C) Schematic illustration of a self-assembled PA nanofiber [20].

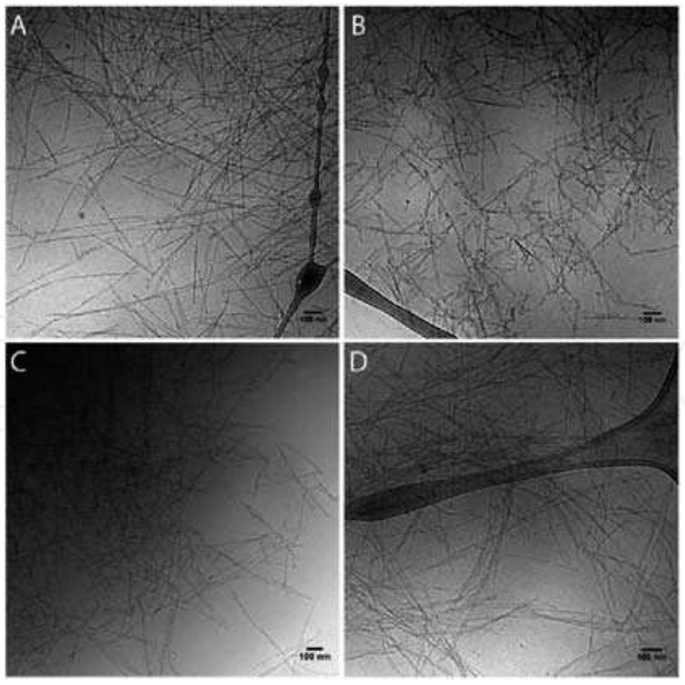

Figure 9. Cryogenic TEM of (A) PA 5, (B) PA 6, (C) PA 7, and (D) PA 8 as 1: 3 w/w mixtures with E2 PA [20].

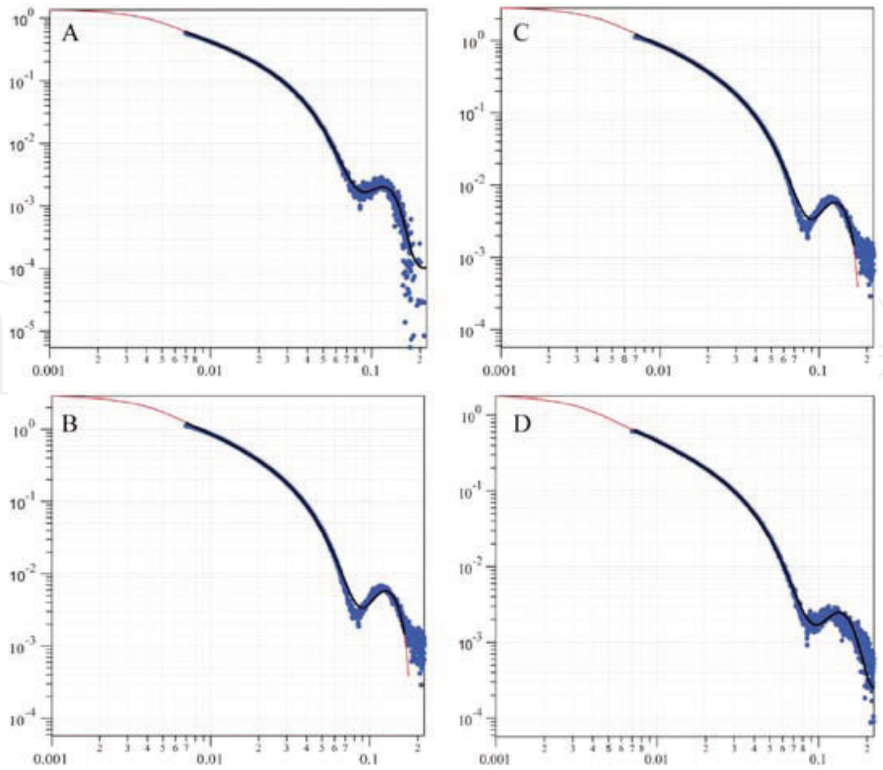

Figure 10. I SAXS profiles of PAs 5-8 (A-D) fitted to a polydisperse core-shell cylinder model. The solid red line represents the best fit to a core-shell cylinder form factor, where the core was allowed to be polydisperse according to a log-normal distribution. The solid black line represents the portion of the curves where fits were performed [20].

PA	5	6	7	8
Mean core radius (A)	12	12	12	12
Radial shell thickness (A)	29	27	25	25
Total diameter (nm)	8.2	7.8	7.4	7.4
Radial polydispersity (σ)	0.3	2.7	0.3	0.28

NaOH without $CaCl_2$ (from Ref. [20]).

Table 1. Selected SAXS data from PAs 5–8 at 0.25% in 4 mM.

3. Concept of evaluation of discrete distribution by SAXS

In this section, the concept of evaluation of the discrete distribution of the size of the nanostructure is explained. As an example, the lamellar model calculations are displayed in **Figure 11**, for which the mathematical equation is [21]:

$$P(q) = q^{-2}L^2[\{\sin(qL/2)\}/(qL/2)]^2 \tag{20}$$

where L is the lamellar thickness and the prefactor (q^{-2}) is the so-called Lorentz factor which is required to randomize the orientation of the lamellar particle. Here, it was assumed that the lamellar particle has infinitely large extent in the direction parallel to the lamellar surface.

Figure 11a and **b** shows the calculated profiles when L was set to 10 and 20 nm, respectively. It can be seen that the characteristics in the shapes of lamellar form factor are similar to the case of spherical form factor. As a matter of fact, many peaks appear. Summing up these two profiles gives the one, which is also shown in **Figure 11c**. This in turn means that the form factor is as shown in **Figure 11c** when the lamellar thickness distribution is as shown in the inset of **Figure 11**. It is noteworthy that the characteristic shape of the one shown in **Figure 11c** (L = 10 nm + L = 20 nm) is similar to the case of **Figure 11a** (L = 10 nm). When the distribution is somewhat modified as indicated in **Figure 12b**, the form factor is dramatically altered to the one as shown in **Figure 12a**. This seems to be no more characteristic form factor. Thus, the experimentally observed form factor can be a fingerprint and the size distribution may be evaluated as far as the shape of the nanostructure can be uniquely assumed.

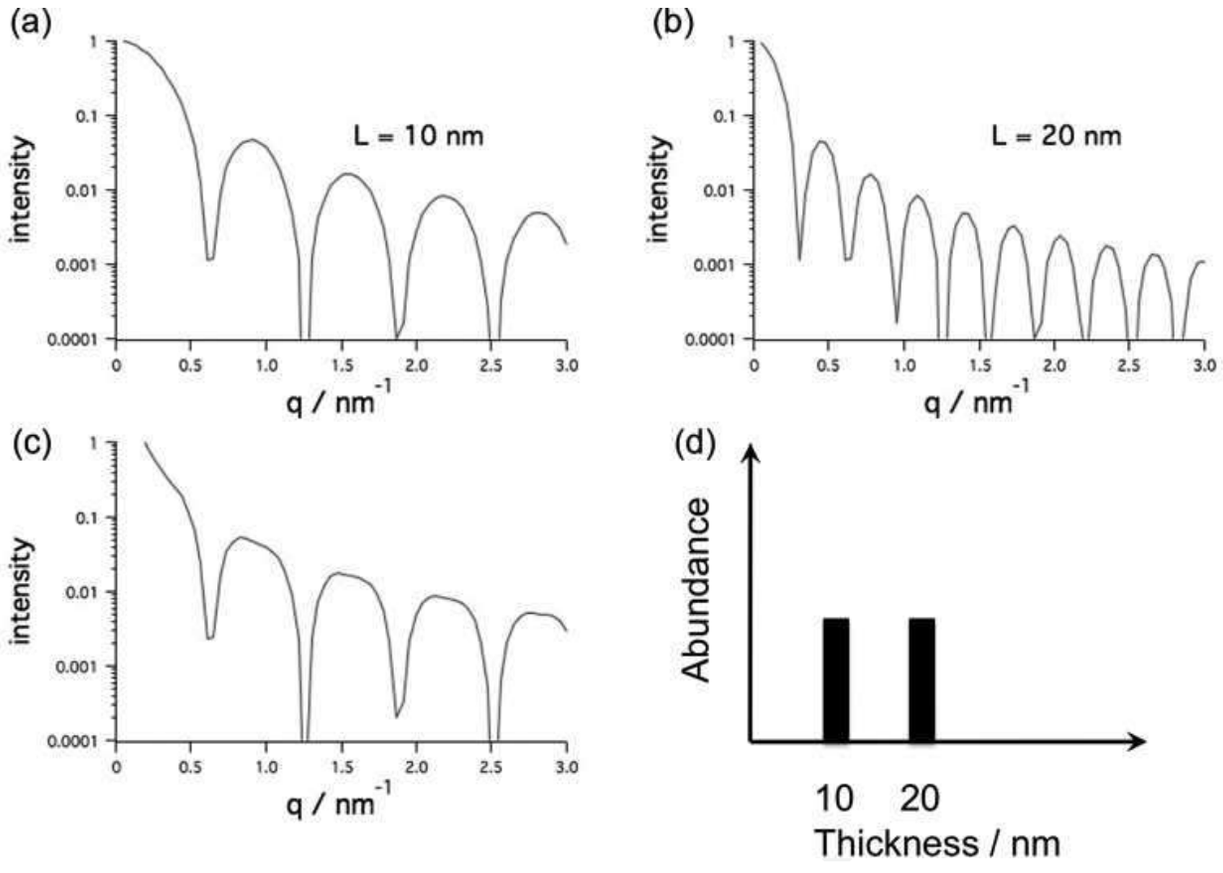

Figure 11. Calculated SAXS profiles for lamellar particle with (a) L = 10 nm, (b) L = 20 nm, and (c) L = 10 nm + L = 20 nm. The inset shows a hypothetical distribution function used for the calculation of the profile shown in **Figure 11c**.

Figure 12c shows one of the typical results of the SAXS profiles for poly(oxyethylene) (PEG), which forms lamellar crystallites. The exact sample used for the result of **Figure 12c** was a polymer blend of PEG with poly (D, L-lactide) (PDLLA), which is a racemic copolymer and therefore amorphous. The compositions of PEG/PDLLA were 80/20 (DL20) by weight. **Figure 12c** shows the result of the SAXS measurement at 64.0°C in the heating process [22].

At the temperature of 64.0°C slightly below the melting temperature of PEG (64.5°C), the typical form factor of lamellar particle was observed first time for the crystalline polymer. It was expected that the thinner lamellar which has a lower melting temperature melted away in the heating process. The thickest lamellae can only survive at the highest temperature and therefore, the thickness distribution became sharp. This may be the reason of the observation of the typical form factor of lamellar particle. As a matter of fact, a very sharp distribution was evaluated as shown in **Figure 12d** by the method described below.

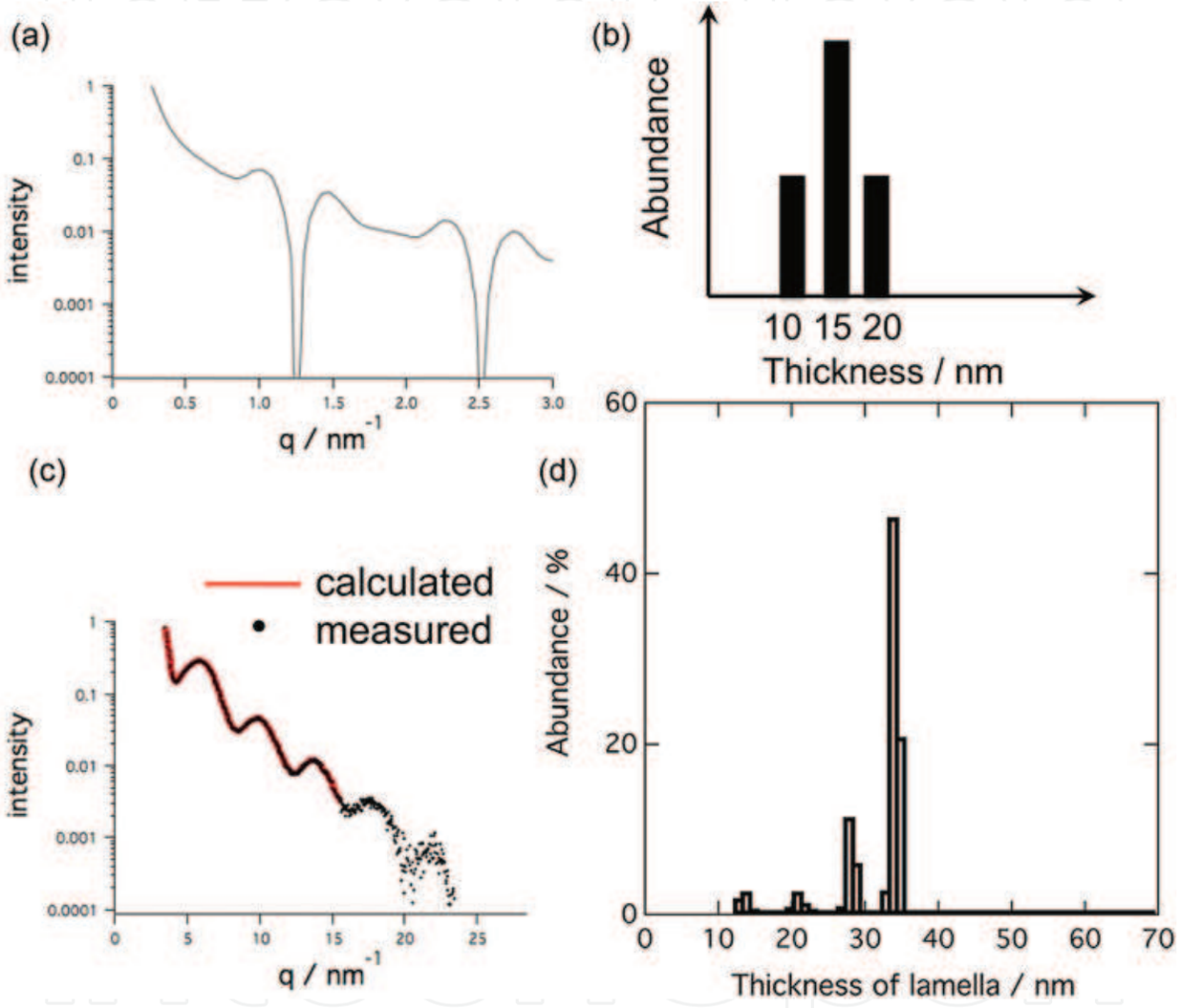

Figure 12. (a) Calculated SAXS profile for lamellar particle with assuming a hypothetical distribution function as shown in part (b). (c) One of the typical results of the SAXS profiles for PEG/PDLLA 80/20 blend at 64.0°C in the heating process. Black dots are for the experimentally obtained SAXS profile, and red curves are the calculated SAXS profile. (d) Evaluated thickness distribution from the result shown in part (c).

Hereafter, the data analysis method for the direct determination of the thickness distribution of lamellar particle is described. The model particle scattering intensity, $I(q)$, with a distribution of thicknesses can be given as:

$$I(\mathrm{q}) = k\Sigma[n(L)P(q)] \tag{21}$$

with $P(q)$ defined by Eq. (20). In Eq. (21), k is a numerical constant and $n(L)$ is the number fraction of lamella with a thickness of L, providing the thickness distribution of lamellae. A protocol was employed to directly determine $n(L)$ by fitting the calculated $I(q)$ from Eq. (21) to the experimentally observed 1D-SAXS profile where the following parameters were being floated as the fitting parameters: the numerical constant k and $n(L = 1$ nm), $n(L = 2$ nm), $n(L = 3$ nm),…, $n(L = 40$ nm) which are the abundance number of particles having thickness L in a step of 1 nm. By this protocol, the best fit was successfully performed, which is shown by the solid curve on the 1D-SAXS profile in **Figure 12c**. Although most of the features seem to be well described by the particle scattering, the first-order peak is not. For some SAXS profiles, the full calculation including the lattice factor $Z(q)$ and the particle scattering can describe the SAXS profile well. The mathematical formulation of $Z(q)$ is [23]:

$$Z(q) = \frac{1-|F|^2}{1-2|F|\cos(qD)+|F|^2} \tag{22}$$

$$|F| = \exp\left(-\frac{g^2D^2q^2}{2}\right) \tag{23}$$

Thus, the thickness distribution as shown in **Figure 12d** was also evaluated. Although such a sharp distribution around $L = 33.5$ nm accounts for the particle scattering dominant SAXS profile, the presence of thinner lamellae is clearly suggested.

4. Widely spread discrete distribution evaluated by SAXS

4.1. Lamellar case

Tien et al. have reported results of comprehensive studies of the higher-order crystalline structure of PEG in blends with PDLLA [22, 24, 25]. For several blend compositions, they have discussed the effects of blending PDLLA on the structural formation of PEG. It is remarkable that they found more regular higher-order structure for PEG 20 wt % composition (DL20) as compared to the PEG 100% sample in the as-cast blend sample (cast from a dichloromethane solution). More interestingly, they reported that the 1D-SAXS profile markedly changed from lattice peak dominant type to particle scattering dominant type when heating the as-cast sample, as shown in **Figure 13**. The compositions of PEG/PDLLA were 100/0, 95/5 (DL5), 90/10 (DL10) and 80/20 (DL20) by weight. **Figure 13** shows the results of the SAXS measurements in the heating process. Based on the results, we have conducted the evaluation of the lamellar thickness distribution in the heating process from the as-cast state up to 64°C and succeeded in showing that the distribution became sharper with the average thickness becoming larger, as shown in **Figure 14**. That study is the first showing quantitative evidence of the well-known concept of 'lamellar thickening' when a crystalline polymer is thermally annealed just below its melting temperature. Tien et al. have also conducted the same evaluation under higher pressure (5 and 50 MPa) [26].

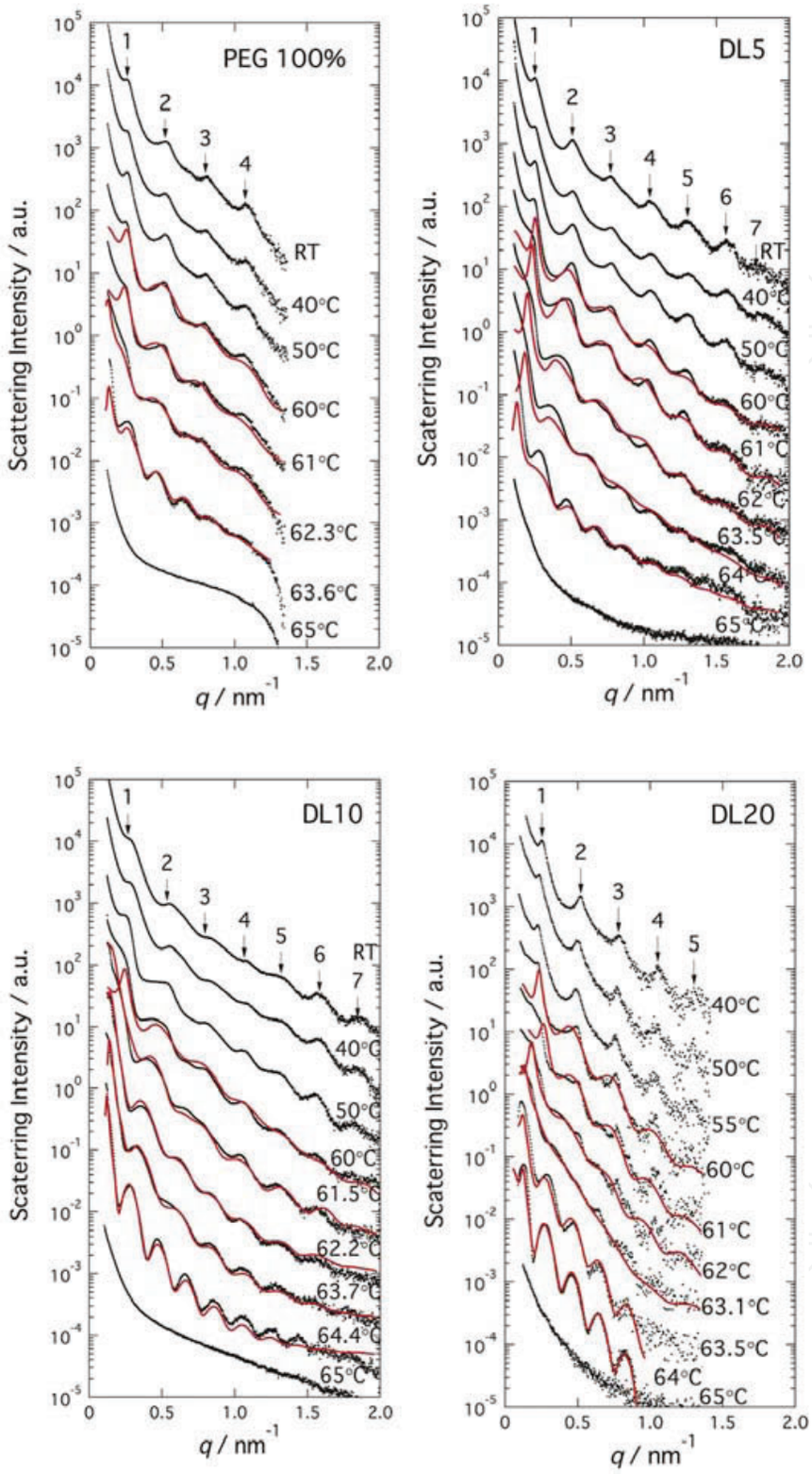

Figure 13. SAXS profiles for PEG/PDLLA blends with 100/0, 95/5 (DL5), 90/10 (DL10), and 80/20 (DL20) by weight. The SAXS measurements were conducted in the heating process. Black dots are for the experimentally obtained SAXS profiles, and red curves are the calculated SAXS profiles [22].

http://dx.doi.org/10.5772/105981

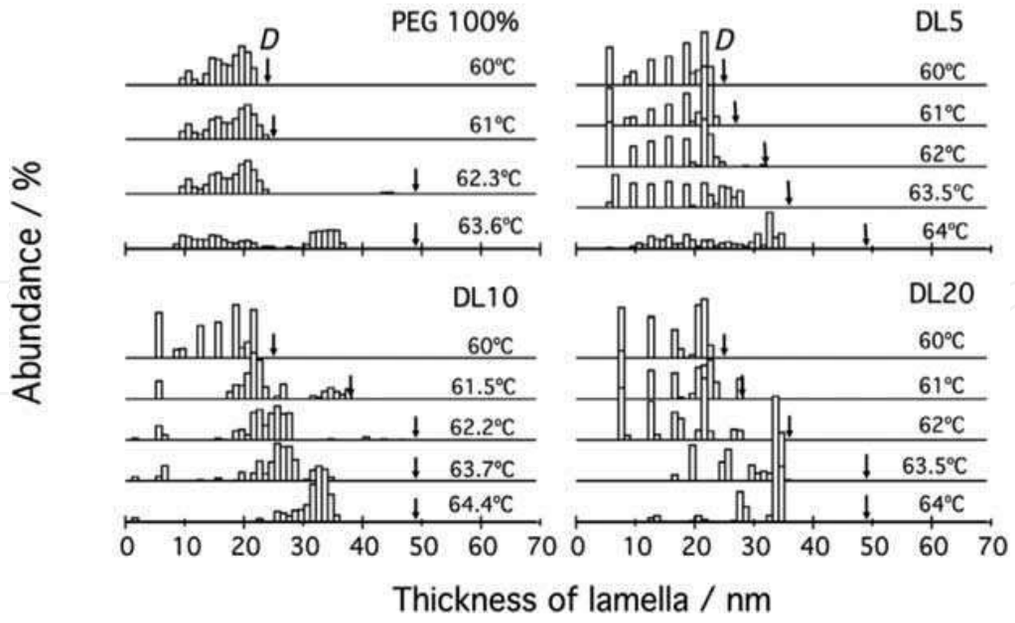

Figure 14. Evaluated thickness distribution from the result shown in **Figure 13** [22].

Jia et al. [27] have recently evaluated thickness distribution of the hard segment domains for supramolecular elastomers (starblocks of soft polyisobutylene and hard oligo(β-alanine) segments). The molecule is a novel type of supramolecule as schematically shown in **Figure 15** where the green chains are soft polyisobutylene. Due to the formation of the lamellar crystallites of oligo (β-alanine) segments, the specimen has rubber-like elasticity, that is, supramolecular self-assembly leads the specimen to TPE. Since such lamellar crystallites can be hardly observed by TEM, the SAXS measurement was conducted. The result is shown in **Figure 16** with the evaluated thickness distribution which is shown in the inset. Almost monodispersed distribution was evaluated with the peak at L = 2.0 nm (inset of **Figure 16**), which is in good agreement with the size of the oligo (β-alanine) contour length. This case clearly demonstrates the significance of the SAXS technique.

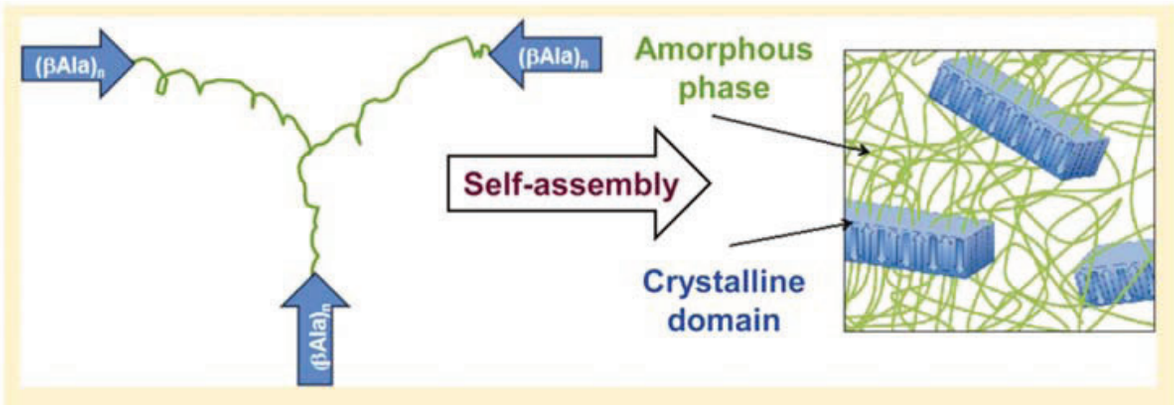

Figure 15. Schematic illustrations for supramolecular elastomers (starblocks of soft polyisobutylene and hard oligo(β-alanine) segments) where the green chains are soft polyisobutylene [27].

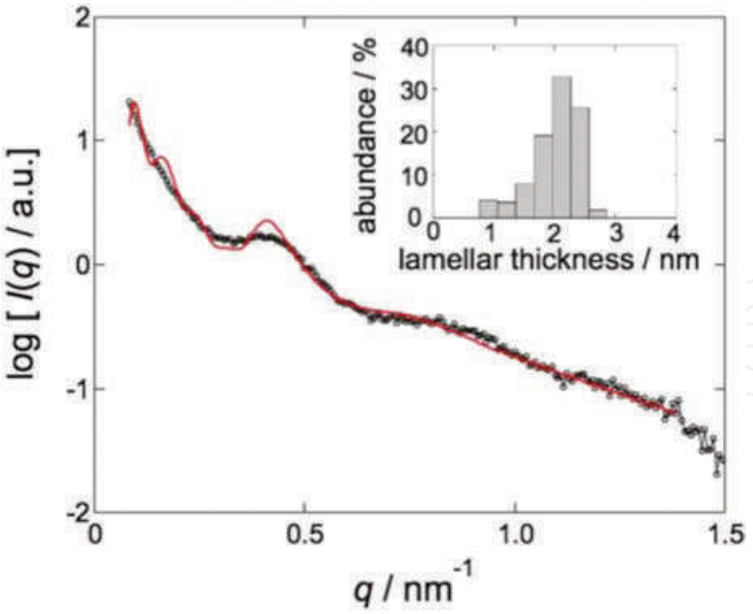

Figure 16. SAXS profile for the supramolecular elastomer schematically shown in **Figure 15**. Black dots are for the experimentally obtained SAXS profile, and red curve is the calculated SAXS profile. The inset shows the evaluated thickness distribution [27].

4.2. Spherical case

In this subsection, the size distribution of nanoparticles is described. Fujii et al. [28, 29] have synthesized novel for sterically stabilized polypyrrole-palladium (PPy-Pd) nanocomposite particles. Such a characteristic particle containing heavy element has recently been attracting intensively general interests of researchers in many fields under the name of element-blocks [30]. **Figure 17** shows a TEM image of these particles with a schematic of the structure. The ordinary 1D-SAXS profiles of 1, 2 and 3% aqueous dispersions of the nanocomposite particles are shown together in **Figure 18a** as a plot of log[$I(q)$] versus log q. This plot clearly shows that the shapes of the profiles are similar. When the curves are vertically shifted, all of the data collapse onto a single curve (**Figure 18b**), suggesting that the nanocomposite particles are dispersed in the aqueous medium without ordering into a lattice, at least up to a particle concentration of 3%. Thus, the 1D-SAXS profile can be attributed directly to the particle scattering (the form factor). Although the TEM results revealed that the nanocomposite particles are not spherical, a mathematical equation describing particle scattering is not available for such an unusual shape of particles. Therefore, a spherical shape is assumed for simplicity. The model particle scattering intensity, $I(q)$, with a distribution of thicknesses can be given as:

$$I(q) = k\Sigma[n(R)P(q)] \tag{24}$$

The form factor, $P(q)$, for spherical particles is given as:

$$P(q) = (4\pi R^3/3)^2[\Phi(q)]^2 \tag{25}$$

and

$$\Phi(q) = 3/(qR)^3[\sin(qR) - qR\cos(qR)] \tag{26}$$

http://dx.doi.org/10.5772/105981

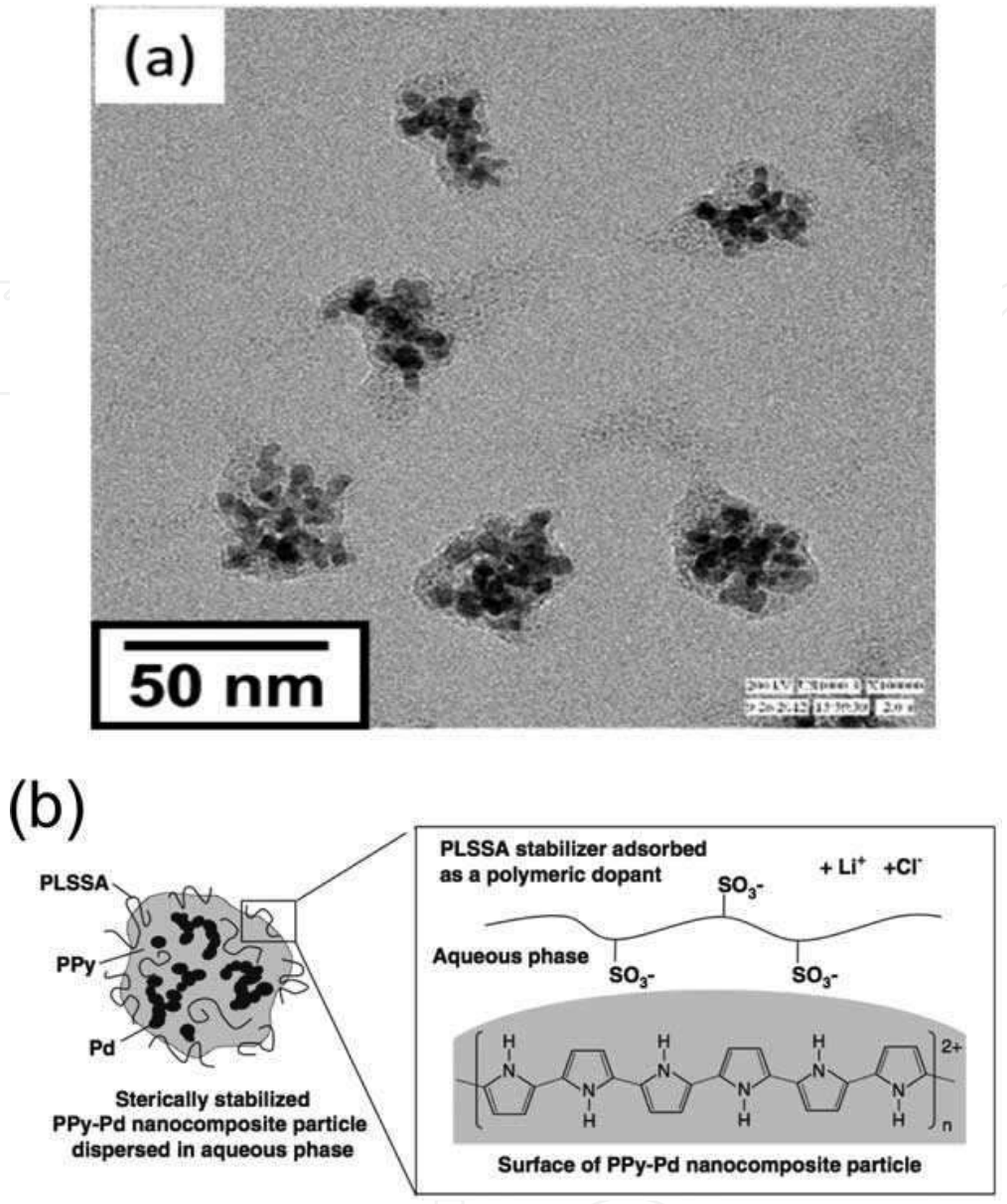

Figure 17. (a) TEM image of sterically stabilized polypyrrole-palladium (PPy-Pd) nanocomposite particles, and (b) a schematic of the structure [28].

In Eq. (24), k is a numerical constant and $n(R)$ is the number fraction of spheres with a radius of R, providing the size distribution of spheres. Attempts to fit a theoretical function given by Eq. (24) to the measured 1D-SAXS profile assuming a Gauss or Schulz-Zimm-type distribution for $n(R)$ were unsuccessful. We then employed a protocol in which $n(R)$ was directly determined by fitting the calculated $I(q)$ from Eq. (24) to the experimentally observed 1D-SAXS profile by the same method as described above for the lamellar case. The best fit is shown in **Figure 18a** with the dotted black curve for the 1D-SAXS profile (3% aqueous solution). The reason of using this profile is because of being most intense and therefore the most reliable. Thus, the obtained particle size distribution is shown in **Figure 19**, where the abundance is shown in the units of vol%, which was calculated by the following equation from the number fraction $n(R)$:

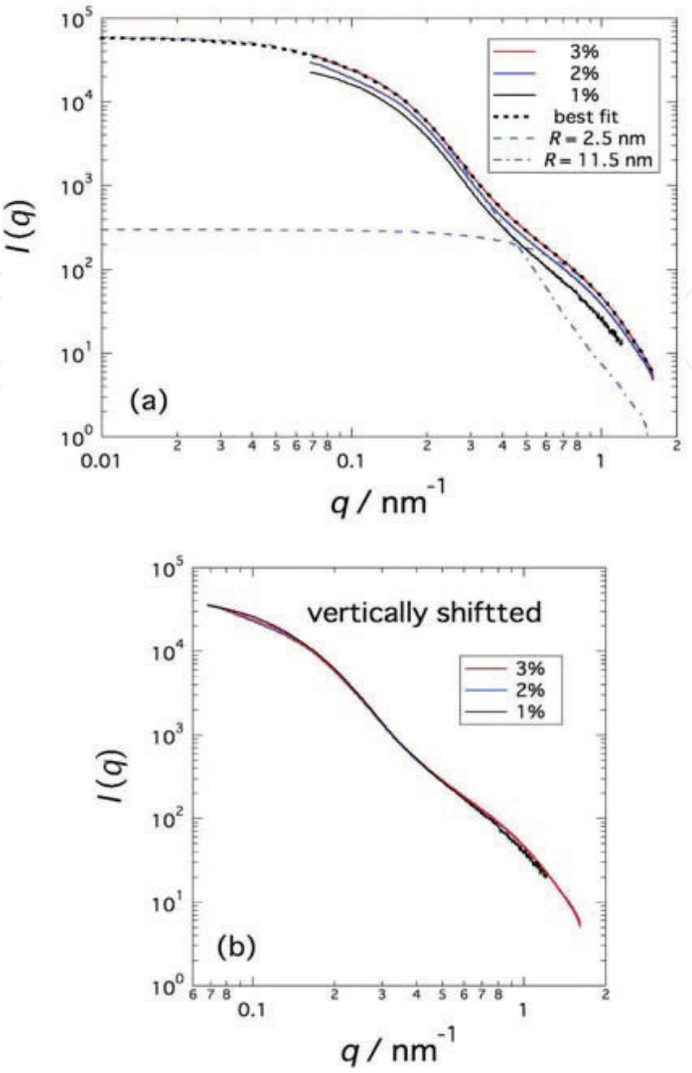

Figure 18. (a) SAXS profiles of 1, 2, and 3% aqueous dispersions of the PPy-Pd nanocomposite particles as a plot of log [$I(q)$] versus log q. The best-fit curve is shown as a dotted black curve on the 1D-SAXS profile for the 3% aqueous solution (most intense and therefore most reliable). (b) Master curve for the SAXS profile obtained by vertically shifting the three 1D-SAXS profiles in (a) (not shifted in q-axis direction) [28].

$$\text{abundance } (vol\%) = n(R)R^3/\Sigma[n(R)R^3] \times 100 \tag{27}$$

Bimodal size distribution was clearly obtained with two peaks at approximately R = 2.5 and 11.5 nm. It is recognized that smaller particles (assuming $n(R)$ with a single peak at approximately R = 2.5 nm) could explain the shape of the SAXS profile in the higher q range (see the broken curve in **Figure 18a**), whereas larger ones (assuming $n(R)$ with a single peak at approximately R = 11.5 nm) characterized the SAXS profile in the lower q range (see the dotted and broken curve). This result does not indicate the real distribution of the PPy-Pd nanocomposite particles themselves, but the additional abundance of tiny Pd nanoparticles existing in the nanocomposite particles. These speculations are confirmed by TEM observations (**Figure 17**), indicating that the average radius was approximately 16 nm with a unimodal distribution and by close examination of the high-resolution TEM image (R = 2.7 nm; **Figure 17**). Thus, it was possible to evaluate not only the size of 'a bunch of grapes' but also the size of all 'grains of grapes in the bunch.'

http://dx.doi.org/10.5772/105981

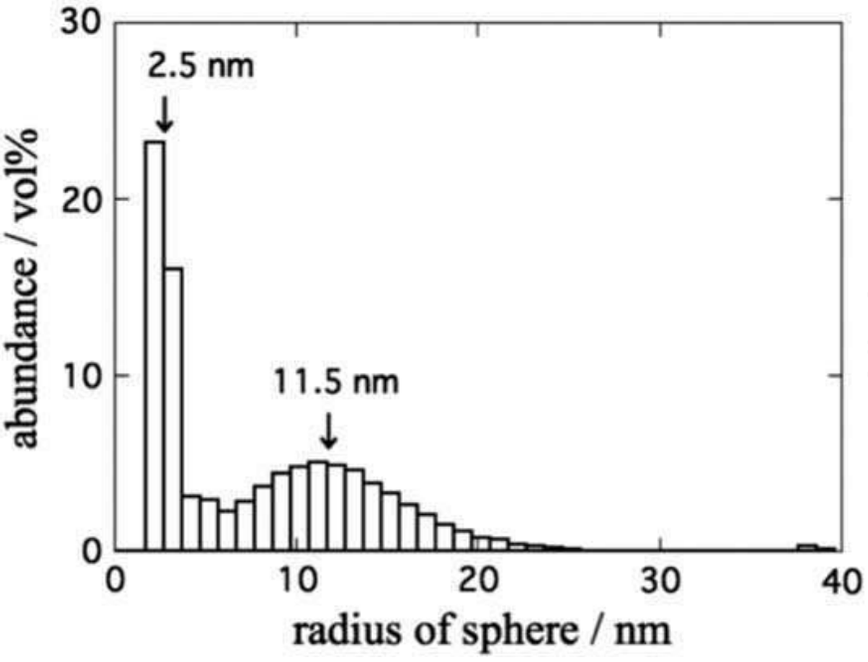

Figure 19. Evaluated particle size distribution based on the result shown in **Figure 18** [28].

Kuroiwa et al. [31, 32] have synthesized novel amphiphilic *N*-isopropylacrylamide (NIPPAm) oligomers with dodecyl groups and carboxyl groups, as shown in **Figure 20a**, by the RAFT polymerization of NIPPAm with *S*-1-dodecyl-*S*′-(*α*,*α*′-dimethyl-*α*″- acetic acid) trithiocarbonate (DTC). It was interestingly found that the DTC-NIPPAm oligomers form network aggregation upon addition of Cu^{2+} ion in an aqueous solution, as revealed by TEM (**Figure 20b** for the dried specimen from an aqueous solution of DTS-NIPPAm35 with Cu^{2+} ions). It seems that the network diameter is somewhat 30 nm or above. There is a possibility to consider that the constitutive unit of the network should be a micelle as schematically illustrated in **Figure 20c**. Since the TEM observation can be only conducted for the dried specimen, the resultant TEM image might be quite different from the real structure in the aqueous media. In order to reveal real structure in the aqueous media, the in situ SAXS measurement was performed at room temperature. Then, the spherical model fitting was applied to the resultant SAXS profile. **Figure 21** shows the SAXS profile with the model form factor. The experimentally obtained SAXS curve (black curve) is available for $q > 0.06$ nm^{-1} and characteristic dent and hump are observed around $q = 0.15$ and 0.50 nm^{-1}, respectively. By assuming the spherical model, the calculated SAXS profile (red curve) can perfectly fit to the experimental one as displayed in **Figure 21**. Thus, evaluated discrete distribution of the radius is shown in **Figure 22**. Here, the main distribution is found around 2–7 nm, implying the cores of the micelles. Because the core contains sulfur atoms, the contrast is considered to be highest and therefore, the core can be the most intense scatterer. This is the reason of observing majority in 2–7 nm in the distribution. This in turn implies that the network aggregation comprises micelles, which can never be detected by TEM. Close examination of the resultant distribution revealed minor abundance around 17 and 21 nm. This agrees well with the least radius of the network aggregation in the TEM observation, as mentioned above. The same distribution is shown in the inset of Figure? with the logarithmic axis for the abundance. Then, it is clear that not only the minor abundance around 17 and 21 nm, but many

minor ones are discernible in the wide range from 17 to 58 nm. As a matter of fact, such big spheres can be occasionally seen in the TEM image (**Figure 20b**). Thus, once again for this kind of complicated aggregation, the method of evaluation of the discrete distribution of size from the SAXS result is approved to be quite effective [33].

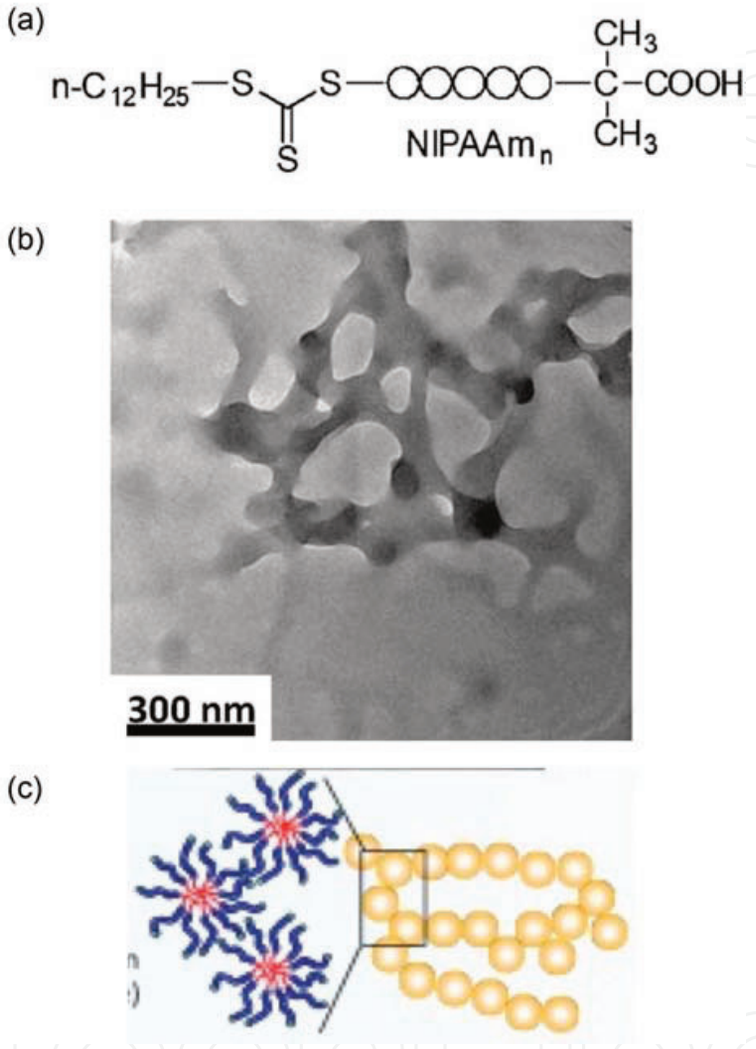

Figure 20. (a) Novel amphiphilic *N*-isopropylacrylamide (NIPPAm) oligomers with dodecyl groups and carboxyl groups. (b) TEM micrograph for the dried specimen from an aqueous solution of DTS-NIPPAm35 with Cu^{2+} ions. (c) Schematic illustration of the micelle network [31, 32].

5. Concluding remarks

In this chapter, we focused on the form factor of a variety of nanostructures (spheres, prolates, core-shell spheres, core-shell cylinders and lamellae). Also getting started with a mono-disperse distribution of the size of the nanostructure, to unimodal distribution with a narrow standard deviation or wide-spreading distribution and finally to the discrete distribution can be evaluated by the computational parameter fitting to the experimentally obtained SAXS profile. In particular, for systems forming complicated aggregations, this methodology is useful. Not only the size

http://dx.doi.org/10.5772/105981

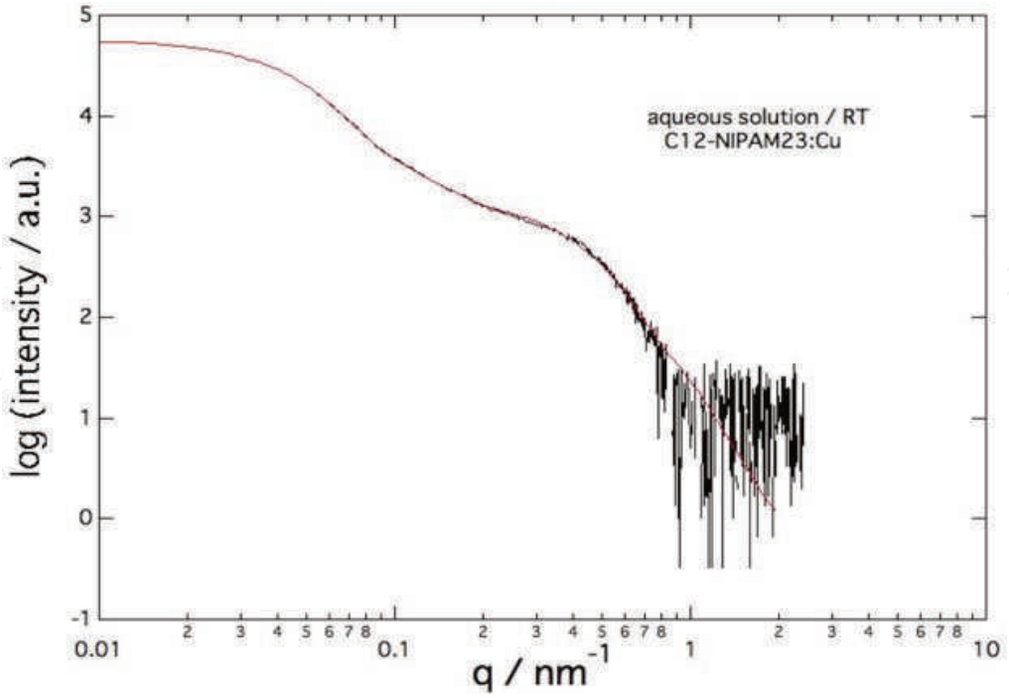

Figure 21. SAXS profile for an aqueous solution of DTS-NIPPAm35 with Cu^{2+} ions with the model form factor. The black curve is the experimentally obtained SAXS profile, and the red curve is the calculated SAXS profile [31, 32].

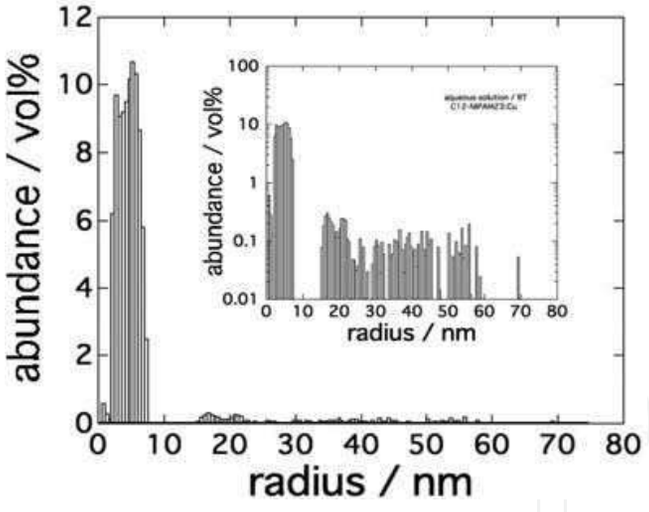

Figure 22. Evaluated size distribution based on the result shown in **Figure 21** [31, 32].

distribution of 'a bunch of grapes' but also the size distribution of all 'grains of grapes in the bunch' can be evaluated according to this methodology. This is very much contrasted to the case of the DLS technique by which only 'a bunch of grapes' is analyzed but 'grains of grapes in the bunch' cannot be. It is because the DLS technique in principle evaluates diffusion constants of particles and all of the grains in the same bunch of grapes diffuse as a whole. Thus, the methodology is important to highlight versatility and diversity in real materials, especially in soft matter,

both in the liquid and in the solid states. At present, however, the shape of the nanostructure is limited in spherical or lamellar. On extending the methodology to the complicated structures such as cylinder, prolate, oblate, or core-shell type, there are tremendous difficulties. For cylinder, prolate, or oblate, difference in the degree of orientation of such particles spoils the methodology such that the size distributions for two principal directions (height and radius for the cylinder case/long axis radius and short axis radius for the prolate and oblate cases) cannot be uniquely evaluated. As for core-shell type particles, the inner and outer radii couple to alter its form factor, so that the size distributions for them cannot be uniquely evaluated either. As a matter of fact, the size distribution is introduced with keeping constant of the ratio of the inner and outer radii for the core-shell spheres [16]. Similarly, for the core-shell cylinders [20], the size distribution in the core radius is incorporated, while the radial shell thickness is assumed to be monodisperse. For more detailed structure analyses, more experimental variations are required to gather information from different kinds of aspects, like the example shown in **Figure 6a** and **b** (parallel and perpendicular to SD). These difficulties should be overcome.

Author details

Shinichi Sakurai

Address all correspondence to: shin@kit.ac.jp

Department of Biobased Materials Science, Kyoto Institute of Technology, Matsugasaki, Sakyo-ku, Kyoto, Japan

References

[1] S. Kobayashi, M. Klaus (Eds.), Encyclopedia of Polymeric Nanomaterials, Springer, New York (2015).

[2] W. H. de Jeu, Basic X-ray Scattering for Soft Matter, Oxford University Press, Oxford, UK (2016).

[3] J. S. Pedersen, Adv. Colloid Interface Sci., 70, 171–210 (1997).

[4] M. Kim, Y. Rho, K. S. Jin, B. Ahn, S. Jung, H. Kim, M. Ree, Biomacromolecules, 12(5), 1629–1640 (2011).

[5] D. Sato, H. Ohtomo, Y. Yamada, T. Hikima, A. Kurobe, K. Fujiwara, M. Ikeguchi, Biochemistry, 55(2), 287–293 (2016).

[6] A. V. Semenyuk, D. I. J. Svergun, Appl. Crystallogr, 24, 537 (1991).

[7] T. Fujisawa, K. Inoue, T. Oka, H. Iwamoto, T. Uruga, T. Kumasaka, Y. Inoko, N. Yagi, M. Yamamoto, T. Ueki, J. Appl. Crystallogr, 33, 797–800 (2000).

[8] U-S. Jeng, C. H. Su, C.-J. Su, K.-F. Liao, W.-T. Chuang, Y.-H. Lai, J.-W. Chang, Y.-J. Chen, Y.-S. Huang, M.-T. Lee, K.-L. Yu, J.-M. Lin, D.-G. Liu, C.-F. Chang, C.-Y. Liu, C.-H. Chang, K. S. Liang, J. Appl. Crystallogr, 43, 110–121 (2010).

[9] T. Sibillano, L. De Caro, D. Altamura, D. Siliqi, M. Ramella, F. Boccafoschi, G. Ciasca, G. Campi, L. Tirinato, E. Di Fabrizio, C. Giannini, Sci. Rep., 4, 6985 (2014). doi:10.1038/srep06985

[10] S. Aida, S. Okamoto, S. Sakurai, J. Masamoto, S. Nomura, Mater. Soc. Res. Int., 7, 234 (2001).

[11] H. Matsuoka, H. Tanaka, T. Hashimoto, N. Ise, Elastic scattering from cubic lattice systems with paracrystalline distortion. Phys. Rev. B, 36, 1754 (1987).

[12] H. Matsuoka, H. Tanaka, T. Hashimoto, N. Ise, Elastic scattering from cubic lattice systems with paracrystalline distortion. II. Phys. Rev. B, 41, 3854 (1990).

[13] T. Kota, K. Imaizumi, S. Sasaki, S. Sakurai, Polymers, 3, 36–50 (2011).

[14] K. Imaizumi, T. Ono, T. Kota, S. Okamoto, S. Sakurai, J. Appl. Crystallogr., 36, 976–981 (2003).

[15] S. Tomita, N. Shimizu, N. Igarashi, H. Takagi, S. Sasaki, S. Sakurai, to be published (2016).

[16] J. Wagner, J. Appl. Crystallogr., 37, 750–756 (2004).

[17] I. Akiba, A. Takechi, M. Sakou, M. Handa, Y. Shinohara, Y. Amemiya et al., Macromolecules, 45, 6150–6157 (2012).

[18] J. S. Pedersen, C. Svaneborg, K. Almdal, I. W. Hamley, R. N. Young, Macromolecules, 36, 416−433 (2003).

[19] Y. Sanada, I. Akiba, K. Sakurai, K. Shiraishi, M. Yokoyama, E. Mylonas et al., J. Am. Chem. Soc., 135, 2574–2582 (2013).

[20] J. B. Matson, C. J. Newcomb, R. Bitton, S. I. Stupp, Soft Matter, 8, 3586–3595 (2012) (and the supporting information).

[21] S. Sakurai, S. Okamoto, T. Kawamura, T. Hashimoto, J. Appl. Crystallogr., 24, 679–684 (1991).

[22] N. D. Tien, T. P. Hoa, M. Mochizuki, K. Saijo, H. Hasegawa, S. Sasaki, S. Sakurai, Polymer, 54, 4653–4659 (2013).

[23] M. Shibayama, T. Hashimoto, Macromolecules, 19(3), 740–749 (1986).

[24] N. D. Tien, T. P. Hoa, G. Kimura, Y. Yamashiro, H. Fujiwara, M. Mochizuki, S. Sasaki, S. Sakurai, J. Phys. Conf. Ser., 272, 012007-1–012007-7 (2011).

[25] N. D. Tien, S. Sasaki, H. Masunaga, N. Shimizu, N. Igarashi, S. Sakurai, Polymer, 55, 2562–2569 (2014).

[26] N.-D. Tien, S. Sasaki, S. Sakurai, Polym. Bull., 73, 399–408 (2016).

[27] J. Scavuzzo, S. Tomita, S. Cheng, H. Liu, M. Gao, J. P. Kennedy, S. Sakurai, S. Z. D. Cheng, L. Jia, Macromolecules, 48, 1077–1086 (2015).

[28] H. Takeoka, N. Fukui, S. Sakurai, Y. Nakamura, S. Fujii, Polymer J., 46, 704–709 (2014).

[29] H. Takeoka, S. Wada, S. Yusa, S. Sakurai, Y. Nakamura, S. Fujii, J. Adhes. Soc. Jpn., 51 (S1) (special issue on WCARP-V), 255–263 (2015).

[30] Y. Chujo, K. Tanaka, Bull. Chem. Soc. Jpn., 88, 633–643 (2015).

[31] K. Kuroiwa, C. Higuma, Y. Shimogawa, H. Hachisako, S. Sakurai, Kobunshi Ronbunshu, 71, 457–466 (2014) (in Japanese).

[32] K. Kuroiwa, Y. Koga, Y. Ishimaru, T. Nakashima, H. Hachisako, S. Sakurai, Polym. J., 48, 729–739 (2016).

[33] K. Kuroiwa, T. Arie, S. Sakurai, S. Hayami, T. J. Deming, J. Mater. Chem. C, 3, 7779–7783 (2015).

Chapter 6

X-Ray Scattering Techniques Applied in the Development of Drug Delivery Systems

Margareth Kazuyo Kobayashi Dias Franco, Daniele Ribeiro de Araújo, Eneida de Paula, Leide Cavalcanti and Fabiano Yokaichiya

Additional information is available at the end of the chapter

http://dx.doi.org/10.5772/65326

Abstract

The advances in nanotechnology have found application in different fields, such as food, agriculture, materials, chemistry, and medicine. However, one of the most important approaches is the development of nanocarriers and, in order to understand their structural organization, different physicochemical techniques have been used. In particular, small angle X-ray scattering (SAXS) and X-ray diffraction (XRD) have given important contribution to the study of organization phase of nanocarriers such as organic/inorganic nanoparticles, micelles, liposomes, cyclodextrins, polymers, and their interaction with drugs and other bioactive molecules. In this chapter, we will present theoretical aspects, experimental design, and the applications of both techniques for the development of delivery systems for bioactive molecules.

Keywords: drug delivery, diffraction, small angle X-ray scattering

1. Introduction

The term nanocarriers have been used to describe colloidal systems (emulsions, nanospheres, nanoparticles, nanocapsules, liposomes, and micelles) and other compounds such as natural, synthetic, organic, or inorganic materials (ceramic, bioglasses, organometallic compounds, carbon or peptide nanotubes etc.) with dimensions smaller than 500 nm for use as biomaterials, depots, implants, biosensors, vaccines, and biomarkers, in chromatography separation, diagnosis or imaging, and drug delivery systems (DDS) for bioactive

compounds such as peptides, proteins, oligonucleotides, nucleic acids, etc., as shown in **Figure 1**. Those carrier systems can be formulated into various preparations including suspensions, emulsions, capsules, tablets, gels, creams, and ointments for parenteral, oral, or topical use [1].

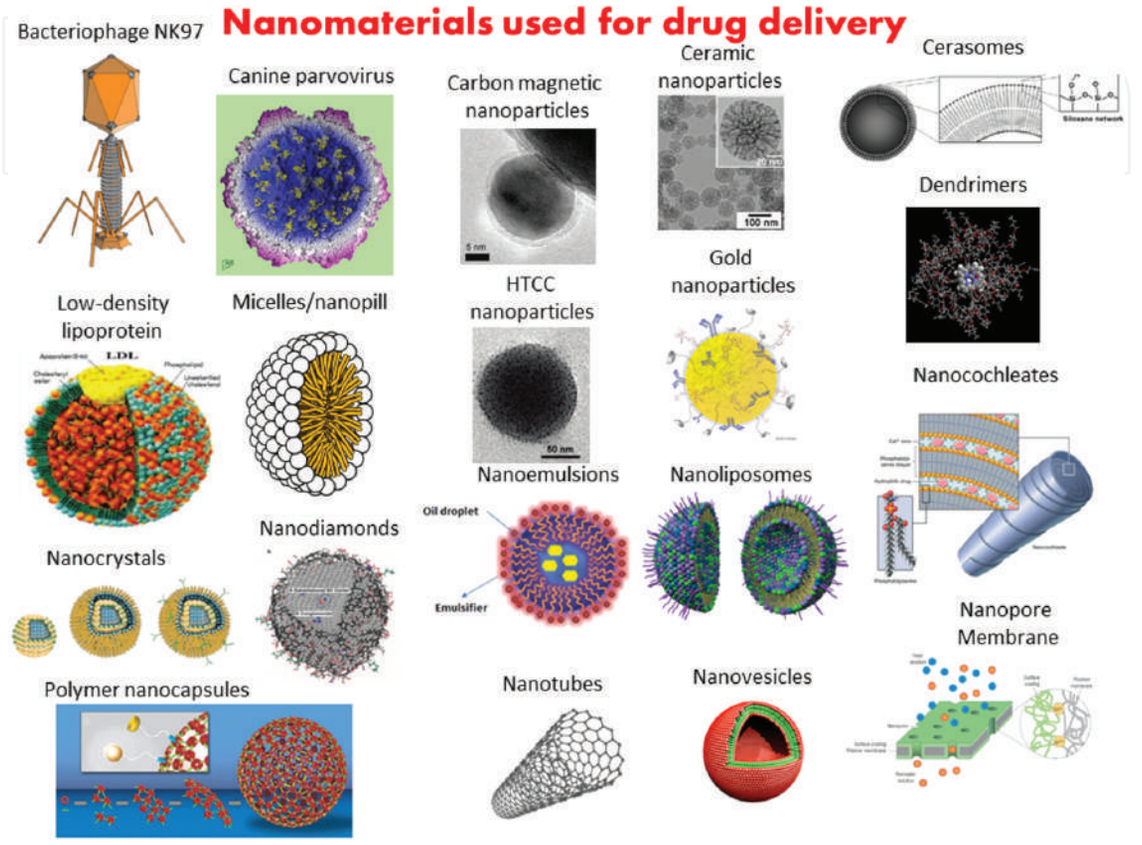

Figure 1. Examples of several drug delivery systems [2–20].

The development of new biomaterials, drug delivery systems (DDS), and modified release pharmaceutical formulations have allowed the modulation of physicochemical and biopharmaceutical properties of the several molecules, enhancing their therapeutic effects and promoting their clinical use. The different drug carriers described in the literature presented results specifically for molecules with limited aqueous or lipid solubility, low bioavailability, low stability, and high local or systemic toxicity [21].

The aim is the encapsulation of the bioactive molecule on a specific carrier destined to deliver it at a controlled rate over a prolonged period. The advantages of some DDS, such as nanoparticles, are their high circulation-residence time and drug bioavailability with enhanced therapeutic efficiency.

Despite several studies that report the physicochemical and biological applications of these nanocarriers, few studies have presented a relationship between their applications and structural aspects. In this chapter, our aim is to describe the basic concepts about X-ray scattering and its application for structural analysis of drug delivery systems.

http://dx.doi.org/10.5772/65326

This chapter explains the basic concepts of X-ray scattering and its applications in drug delivery systems. The basic equations for converting information obtained during the measurements in structural parameters of the object are also presented. We shall restrict ourselves to coherent and elastic small-angle X-ray scattering (SAXS), which is used in structural studies of soft condensed matter and in the X-ray diffraction (XRD) technique.

2. SAXS: small angle scattering technique

2.1. Introduction

Among drug delivery systems (DDS), carriers such as liposomes, micelles, hydrogels, and several kinds of hybrid organic-inorganic nanoparticles [22] can be found. For an effective or stable carrier, the colloidal size, which goes approximately from 1 nm to 1 μm, is an important criterion to select the delivery system that can permeate tissues, circulate with body fluids, or interact with cell membranes. Therefore, the structure is directly correlated with each function and the structural characterization of colloidal systems is in the range of the electron microscopy and X-ray scattering. In this study, we are going to discuss about small angle X-ray scattering (SAXS).

Unlike many other characterization techniques, the success of the SAXS study will highly depend on the prior knowledge available about the system. It means that one has to study thoroughly the sample preparation history, particle morphology, size distribution, aging stability, etc., before proposing SAXS method. The size distribution in the range of some hundreds of nm can be characterized by dynamic light scattering (DLS) [23] and the results can give a hint about agglomeration of the colloidal system that can favor polydispersity, which causes trouble in the resolution of the scattering signal in some cases. Mapping the aging stability is a crucial task in colloidal studies in order to have a fair referential for comparing a series of samples. Aging of colloidal systems can promote agglomeration or crystallization or even degradation and for each case, there will be a different scattering pattern. Morphology, studied using electron microscopy, prior to SAXS measurements, promotes an easier startup on the SAXS modeling and simulation. Fragile organic colloidal systems are better visualized through cryo-TEM (transmission electron microscopy) or cryofracture microscopy [24]. It is also import to know about the surface electric charges of the particles, through Zeta potential measurements [25], prior to SAXS measurements in order to facilitate the understanding of the interaction among all the sample constituents, which helps to build the most likely model structure to simulate the scattering intensity.

The SAXS technique is a nondestructive method and the experiment of scattering is relatively simple and fast. All the hard work will be charged on the treatment and analysis of the acquired data. Measurements taken for few days in a synchrotron lab will be enough for one whole year of analyzing data. Thus, the more you know about the system prior to the measurements, the more precise will be the experiment and the earlier you will be compensated by the information that can be determined through SAXS study.

2.2. Elements of SAXS theory

There are several good references for studying basic SAXS theory; the most popular is the book of Glatter and Kratky [26]. For amphiphilic systems, it is worth to check the article, also from Glatter, published in 1991 [27]; the work from Kratky on biological macromolecules, including some aspects from neutron scattering [28]; and more recent studies from our collaborators Trevisan et al. [29], showing the SAXS analysis for an example of modified liposomes after shearing preparation process, published in 2011; and the article of Oliveira et al. showing an efficient method to model and simulate SAXS intensity from unilamellar and multilamellar liposomes [30].

The SAXS technique comes from the fact that X-rays can interact with the electrons of the materials. When X-rays strike any matter, part of the energy is absorbed or transmitted. However, the part of the energy that is interesting for this technique is the one that scatters elastically (conserving the original frequency) depending on the structure of the material. The word "scattering" is already explaining everything about the method: instead of passing through the material, some photons are deviated (scattered) after the interaction with the electrons. The angle between the original direction of the photons and the deviation is called the scattering angle. The structure dimensions of the colloids are in the very size limits of the SAXS technique. The bigger the scattering objects, the smaller will be the scattering angle; this is the reason for calling this technique "small angle" scattering in contrast with the "wide angle" scattering used to study atomic distances.

The aim of the method is to study the scattering angle, or the scattering vector $\vec{q}$, in order to learn the characteristics of the object that caused the scattering. In this technique, the object is just a bunch of electrons with some structure. SAXS will give knowledge of the electronic density of the material and its spatial organization.

After X-rays strike the sample, the amplitude $A(\vec{q})$ of the scattered wave in the direction of the scattering vector $\vec{q}$ is represented by the expression:

$$\boldsymbol{A(\vec{q}) = \rho(\vec{r}) e^{-i\vec{q}.\vec{r}}} \tag{1}$$

where $\rho(\vec{r})$ is the average electronic density of the system and $\vec{r}$ is the position of one atom of the material. The total amplitude scattered by all atoms of the material will be represented by the following expression:

$$\boldsymbol{F(\vec{q}) = \int \rho(\vec{r}) e^{-i\vec{q}.\vec{r}} d\vec{r}} \tag{2}$$

which one can recognize as the Fourier transformation of the electronic density. The inverse Fourier transformation would yield the electronic density of the material, which is the very

subject of the study. But the SAXS experiment provides only the intensity of the scattered wave, which is the square modulus of the amplitude of the wave:

$$\boldsymbol{I(\vec{q}) = |F(\vec{q})|^2} \tag{3}$$

Extracting the electronic density of the material from the intensity $I\left(\vec{q}\right)$ is not a straight forward task like the inverse Fourier transformation; it does not give a unique solution because we lost information of the phase of the wave when we squared the modulus; and that is why we need the support of the complementary techniques to find a reasonable model for the electronic density of the material.

On calculating the square modulus of the wave amplitude of Eq. (3), it could be understood that the expression of the intensity will be dependent not only on the electronic density of one point of the structure, but there will be a crossing term indicating that the intensity is the sum over the pair distance distribution function (PDDF) of the system, which expresses a contrast of the electronic density. This aspect is better explained with some examples of colloidal systems that naturally have this contrast of electronic density, for example, the contrast of electrons in proteins and the solution in which they are embedded; or liposomes and the buffer where they are dispersed; or even the contrast between the hydrogels and the pores that they form.

As the interaction with electrons is the origin of the phenomenon, the more electrons the materials have, the higher will be the intensity of the SAXS signal. Organic molecules have low electronic density compared to inorganic materials, so the signal is weak and the experiment need high brilliance sources like synchrotron facilities or lab equipment with enhanced optics for the best performance.

2.3. Experiment

The routine of the experiment is as follows:

Data acquirement: a sample is kept in front of the X-ray source and the scattering intensity at all angles is collected by a detector. Several facilities are prepared with special sample holders, environment conditions, *in situ* parallel techniques, and efficient detectors, as shown in **Figure 2**.

Data treatment: the scattering curve is recovered after data treatment which removes the background scattering caused by possible air gaps, windows, slits, or other parts of the instrumentation. Vacuum chambers are strategically placed to remove air gaps and light materials as beryllium, mica, and polymer films are used as windows to minimize spurious scattering.

Modeling: from the results of complementary techniques the parameters such as particle size, interaction among compounds, crystallization, polydispersity, etc., will help to build a model for the scattering object. For example, one can take a vesicle as a core of water surrounded by lipid bilayers and this model is known as core-shell structure. The size of the core and shell,

as well as the shape of objects interacting with this core-shell phase or the particles that can exist dissolved or crystallized in water, will all be a part of the model. There are several known models to start the approach of the scattering object, for instance, hard or hollow spheres, cylinders or other shapes, and also combined models for polydispersed systems. The scattering of these objects are called form factor scattering in contrast with structure factor, which is related to the periodicity of the shapes that can exist in some systems, for example, in multi-layered liposomes.

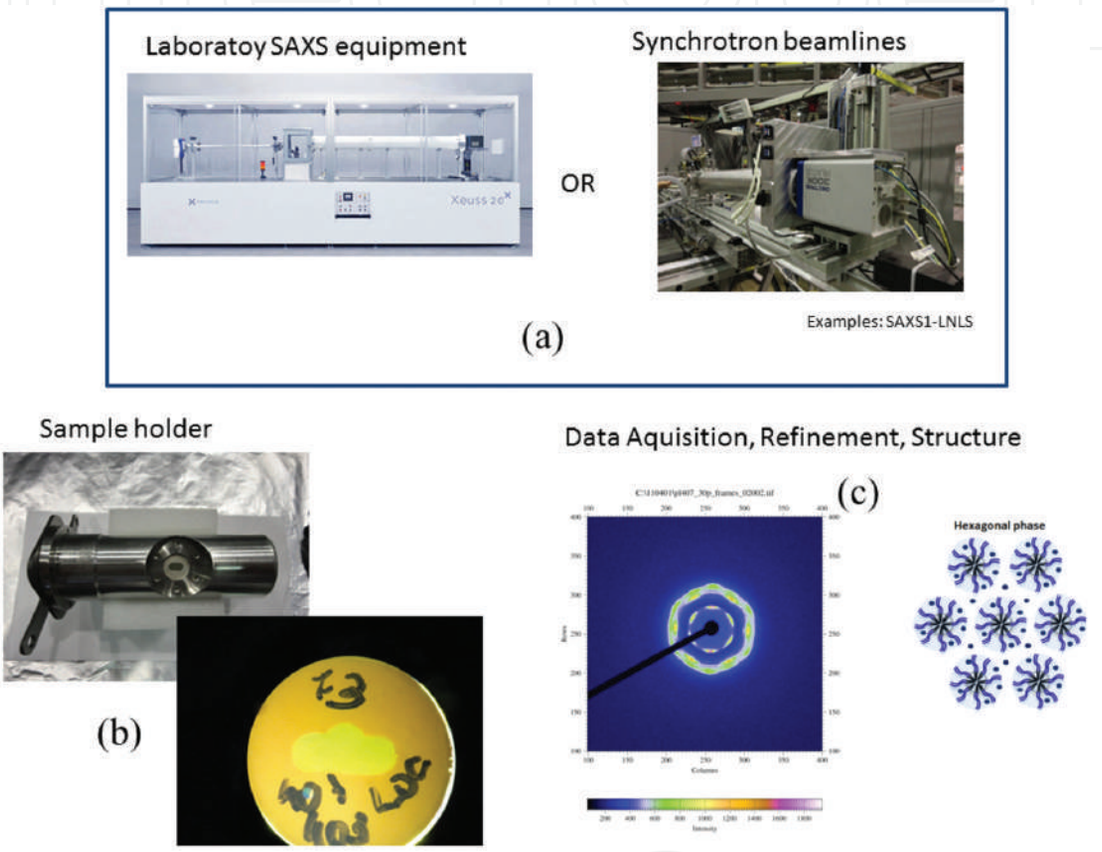

Figure 2. (a) Laboratory SAXS equipment or Synchrotron SAXS beamline can be used to characterize drug delivery systems. (b) Sample holder pictures; (c) some results from poloxamer systems used as drug delivery systems obtained using the SAXS technique [31].

Simulation: after having a model one can calculate the scattering intensity of the model, which is easier if done by computing programs. There are several software tools on the market for SAXS analysis that offer ready-to-use form factors like the ones that we commented before: hard spheres, core-shell, etc. Some software tools even offer possibilities to build your own form factor, considering more complex models.

Fitting: the final step is to compare the simulated scattering intensity with the experimental data. If they fit together, this is the end of the process and one can assume that the chosen model is a reasonable structure supported by all experimental results, not only SAXS, but everything else that helped to build the model. If the simulation does not fit the experimental

data, one can make adjustments on the model, make another simulation and compare again until it fits as good as they want.

In the study of Brzustowicz and Brunger [32], they used a model of hard spheres to fit the dispersion of stearoyloleoyl phosphatidylserine (SOPS) micelles in buffer. This study used a monodisperse micelle sample with the main purpose to propose a different approach for analyzing lipid bilayer SAXS data. The graph of **Figure 3** of that paper shows a perfect fitting between calculated and experimental data. The results were good to determine the size of the inner core of the liposome and the electronic density profile across the membrane.

A successful SAXS analysis was reported in the work of some collaborators Gasperini et al. [33] after Balbino et al. [34]. In both cases, a biopolymer was inserted in liposome dispersions, hyaluronic acid (HA), and DNA, respectively. The results indicate that there are similarities at low concentration of incorporation of polymer inside the liposome dispersion. The negatively charged polymers bonded together neighbor unilamellar cationic liposomes like an electrostatic plastic glue. At higher concentrations of polymer, one can observe distinct behavior for these two biopolymers: DNA succeeded to disrupt the lipid membrane promoting the organization of multilamellar liposomes; and HA was able to coat individual unilamellar liposomes stabilizing the dispersion.

The SAXS analysis of these two studies, together with the results of the complementary techniques, was able to reveal all these details. For this, the liposome preparation was carefully controlled to have minimum polydispersity and the systems were studied strictly under the aging stability period. Several methods were used as complementary techniques such as DLS, zeta potential, TEM, cryo-TEM, and chromatography to help build the structure model to calculate the simulated scattering to be compared to the SAXS experimental data. Reasoning aspects were considered to minimize fitting parameters to increase the reliability of the results.

For other nanocarriers, such as thermosensitive poloxamer (or Pluronics® -PL)-based micelles and hydrogels (see **Figure 3**), SAXS technique have presented important contributions for understanding the structural changes after the incorporation of drugs/carriers or the formation of systems composed of PL with different hydrophilic-lipophilic balance (HLB).

SAXS studies have reported the formation of wormlike micelles for PL-P84 [35]; the gelation mechanisms and micelle packing under hexagonal and body-centered cubic phases for PL-P85 and PL-F88, respectively. However, for the PL-F88/PL-P85 mixture, the destabilization of the hexagonal phase after PL-F88 addition [36], a PL with higher HLB (28) compared to PL-P85 (16) was observed [37]. Other authors also reported SAXS analysis for PL-based binary hydrogels (PL concentrations ranging from 20 to 30% m/v) with different HLB values, such as PL-F127/PL-F68 [38] and PL-F127/PL-L81 [39], being observed in the formation of a hexagonal phase at physiological temperature and their purpose as sumatriptan and ropivacaine delivery systems for application by infiltrative routes. However, for fluid systems (with PL concentrations lower than 18% m/v) the binary micelles composed of PL-F127/PL-L81 presented a lamellar phase structural organization, even after the incorporation of the drug chlorpromazine [40].

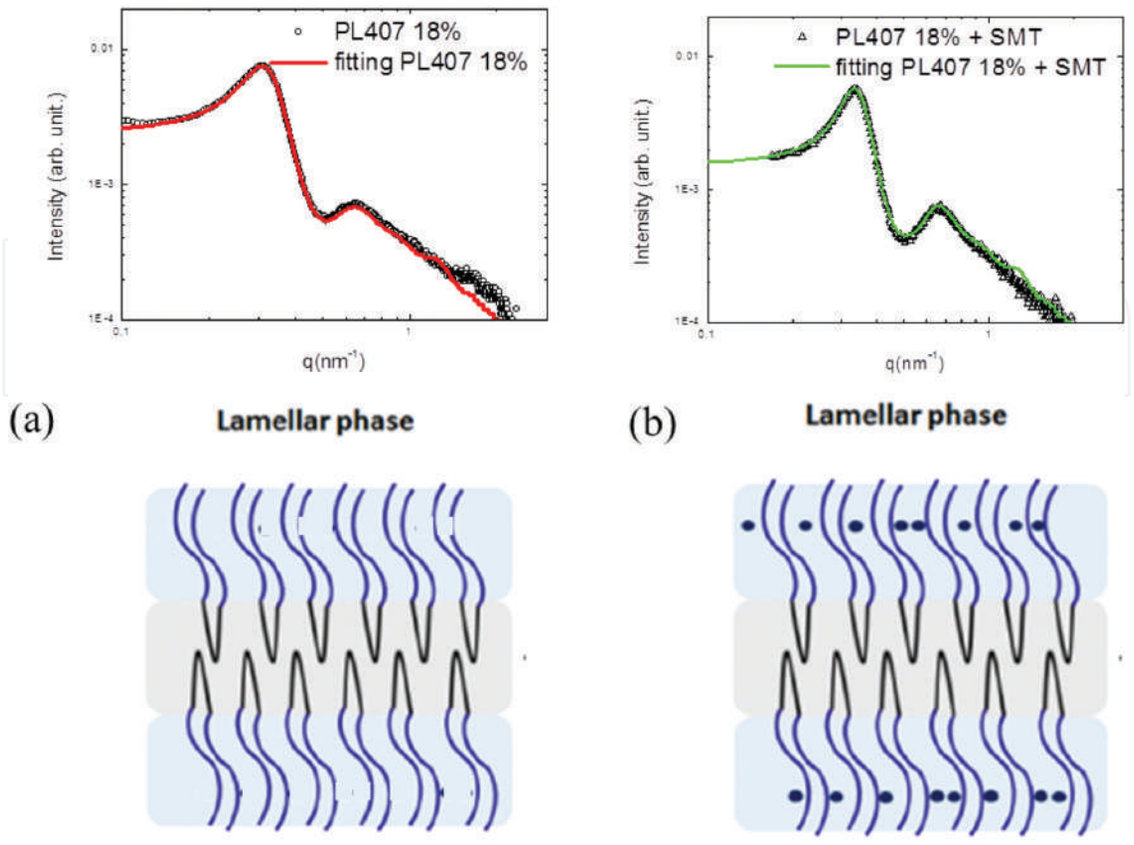

Figure 3. Example of successful SAXS analysis of a drug delivery system based on poloxamers (a) poloxamer without drug; (b) poloxamer with sumatriptane (SMT).

In fact, the drug incorporation of PL-based systems, studied by SAXS, has been highlighted in the literature. In a recent work, Avachat and Parpani [41] described the formulation of liquid crystal nanoparticles for efavirenz oral delivery. The study showed the formation of cubosomes after the incorporation of PL-F127 and phytantriol, a cosmetic ingredient. Chen et al. [42] studied the acetaminophen and bifonazole crystallization mechanism within polyethylene glycol (PEG), polypropylene glycol (PPG), and PL-F127 matrices, observing an improvement of crystallization rate for both drugs.

Another innovative approach relates to the combination of different carrier systems (natural and synthetic, for example) that perform different functions, usually synergistic, in the same pharmaceutical formulation. These new carriers, hybrid systems, can provide (in combination) levels of structural organization and different biopharmaceutical properties of the individual carriers, being used as a strategy to overcome limitations in relation to the physicochemical properties (such as aqueous solubility), pharmacokinetic (control local absorption and/or uptake to the bloodstream), pharmacodynamic (increased drug duration of action) or toxicological properties (improvement in biocompatibility, reduced local and systemic toxicity) [43, 44]. In this sense, the interactions and the structural patterns formed between PL and cyclodextrins, inorganic nanoparticles, and natural or synthetic polymers have been described in the literature.

SAXS studies revealed a face-centered cubic phase for PL-F127 hydrogels (30 wt%) after interaction with PEG 6000 or PEG 35000 and polyvinylpirrolidone [45]. On the other hand, the PL supramolecular structure was destabilized after incorporation of Fe_3O_4 nanoparticles into PL-F108 hydrogels, showing that the thermogelation is due to the clustering of nanoparticles into a fractal network [46]. In a different manner, a cubic symmetry was observed by SAXS characterization of the systems composed of ordered mesoporous silica nanoparticles in PL-F127 hydrogels [47].

For other nanocarriers, such as cyclodextrins (CD), different structural arrangements have been described, being also related to the delivery capability of those systems. Simões et al. [48] reported the development of a syringeable hydrogel composed of PL-F127 and α-CD for the delivery of vancomycin. In others reports, the incorporation of α-CD, studied by SAXS, showed a significant change on gelation behavior of PL-F68 and PL-F127 due to the formation of polypseudorotaxane (interaction of the hydrophobic PL unimers with the hydrophobic cavity of CDs, stabilized by noncovalent bonds, van der Waals forces, and interactions between the hydroxyl groups of adjacent CDs and hydrophilic polyethylene glycol polymer unimers) supramolecular complexes, in a similar manner observed in the interaction between β-CD and PL-F108 [49, 50].

3. X-ray diffraction

3.1. Introduction

One of the biggest challenges of the pharmaceutical science is to understand how the drugs interact with the cells in the body. This study is directly linked to physical and chemical properties of the drugs and the drug delivery systems. Therefore, it is important and necessary to use appropriate techniques for characterization, suitable for the development and improvement of the efficacy of the drugs.

For this reason, X-ray diffraction techniques stands out amongst several characterization techniques to distinguish the solid forms, like salt, polymorphs, solvates and cocrystal, and amorphous forms. X-ray diffraction provides information about the long ordering crystalline samples and also short ordering in vitreous or amorphous materials. This technique helps to relate the X-ray diffraction patterns with the structural ordering or disordering in materials science. It is worth to note that there is a clear difference between the crystalline materials, and amorphous and vitreous materials when observed via X-ray diffractometer. In the X-ray diffraction pattern for crystalline materials, several sharp peaks can be observed. On the other hand, for vitreous or amorphous materials the diffraction pattern display typically three or less halos (large peaks).

In 1999, Wunderlich [51] proposed a classification system based on the structural ordering and molecular packing present in the organic forms using three ordering parameters: translation, orientation, and conformation, as summarized in **Table 1**.

Solid form	Translation	Conformation	Orientation
Crystal	Long order	Long order	Long order
Condis Crystal	Long order	Short order	Long order
Plastic Crystal	Long order	Short order	Short order
Liquid Crystal	Short order	Short order	Long order
Vitreous or amorphous	Short order	Short order	Short order

Table 1. Classification system of solid forms as described by Wunderlich [51].

Solid-form crystals with a long ordering structure can be indexed characterized using X-ray powder diffraction technique (XRPD) due to its unique combination of order parameters. Although the solid forms of amorphous and vitreous materials do not exhibit any long ordering structure, they can be identified and characterized by their local molecular (short) ordering.

Some applications of X-ray diffraction techniques used to analyze the properties of the solid state of the drugs are: (1) characterizing the ordering in the active pharmacological ingredient (API); (2) identifying the existence forms in the API; (3) determining the solid form of API in the final drug product; (4) determining the physical and chemical stabilities; (5) identifying the components existing in the drug product; (6) detecting impurities or contaminants in the drug product; (7) monitoring changes in the sold form of the drug due to the fabrication; and (8) analyzing quantitatively and qualitatively the final drug product.

Based on the sensitivity of the technique to the ordering of structure, with appropriate data obtained from XRPD, it is possible to determine the structure of the solid forms and also the packing of the molecules in the solid. This information contributes significantly in the understanding of the chemical content in the solid state of the drug. Moreover, it is also important from the regulatory perspective.

3.2. Elements of diffraction theory

The X-ray diffraction technique measures the X-ray photons after the collision with the electronic cloud of the sample that changes the photon trajectory, though keeping the same phase and energy of the incoming photon. This is the key concept of the coherent elastic scattering process.

In organic samples, there are some specific facts that must be considered:

1. The application of a mathematical simplification known as first Born approximation is important and useful in the explanation of the X-ray diffraction process.

2. As expected, the interaction of the solid forms in the organic samples with incoming X-ray beam is weak and the amplitude of the multiple radiation scattering is almost negligible when compared to the simple radiation scattering.

http://dx.doi.org/10.5772/65326

3. In the presence of crystal defects, grain boundary or disordering systems, the multiple radiation scattering become even less significant.

Based on these considerations and their limits, we can model the process of diffraction as a Fourier transform of the electronic density inside the sample.

While each atom is considered a specific source of scattering process, the molecules can also be reduced to specific sources of scattering, considering that the distribution of the electronic density of a collective set of atoms is the sum of electronic density distribution attributed to centralized atoms individually.

Although the atoms in a molecule are not necessary the same as the free atoms, they are frequently considered as being free atoms. In this way, the ordering of the specific centers of scattering in the real space produces a group of diffraction events in the reciprocal space that corresponds to the intensity of the peaks.

A d spacing between the punctual centers (molecules) in the real space corresponds to a peak of the $\frac{2\pi}{d}$ spacing in the reciprocal space (also called Q-space).

As the Fourier transform can be applied in any molecular translational ordering that exists inside a solid form, the diffracted peak positions can be expressed in terms of d-space, Q-space or, more common, in 2θ.

In order to cause a constructive interference of the scattered waves, it is necessary that the Bragg's law be obeyed. The Bragg's law relates the X-ray scattering angle θ with the d -spacing parameter, as shown in **Figure 4**.

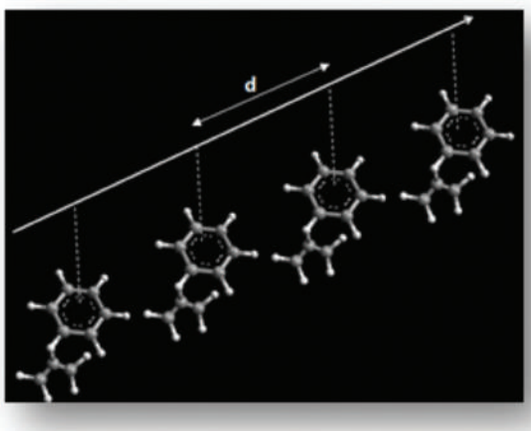

Figure 4. Representation of a simple periodic array of an organic molecule with a single orientation and conformation. The molecules are periodic, separated by a constant spacing d.

$$n\lambda = 2d \sin\theta \tag{4}$$

where λ is wavelength of the incident radiation; n is an integer number; d is interplanar distance to a set of hkl planes of the crystalline structure; θ is X-ray incident angle, as shown in **Figure 5**.

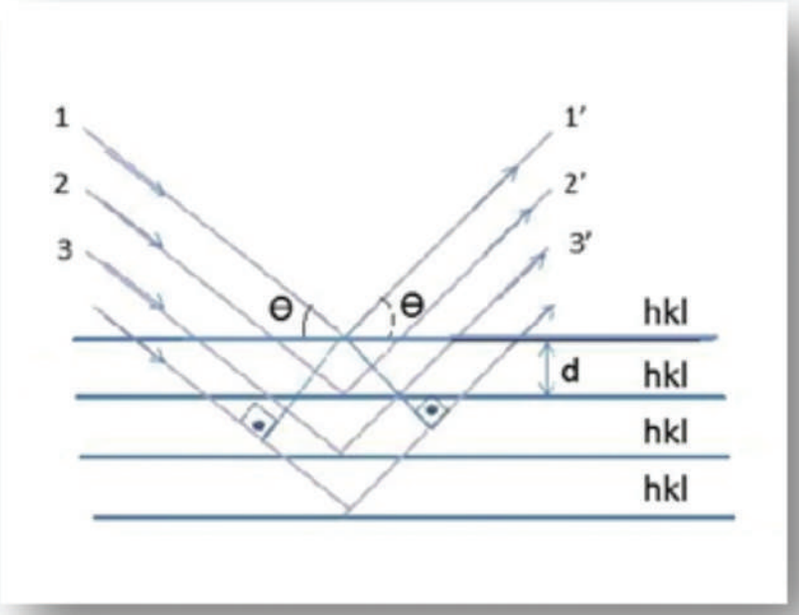

Figure 5. Schematic representaion of the Bragg's law for the X-ray diffraction.

The samples analyzed by the X-ray diffraction technique can be in the powder form or solid with plane surfaces.

Analyzing the diffractogram of a polycrystalline sample, we verify that the peaks related to different set of planes show different intensities. If we build a diffractogram using just geometric aspects (Bragg's law), we will expect that all the peaks display the same intensity since all of them are subjected to constructive interference.

However, there are several physical aspects that influence the intensity of the peaks in a diffractogram, such as:

- Atomic scattering factor (this value indicates how an atom can scatter to a certain angle in a certain wavelength).
- Structure factor (quotient of amplitudes of scattered waves by all the atoms in a unit cell and the amplitude of the scattered wave by on electron).
- Multiplicity factor (there are planes that, for having the same interplanar distance, scatter to the same peak. This is the case, for instance, of 100, 010, and 001 planes in a cubic cell. Adding also the planes, qith −1 instead of 1, we have in total six planes contributing to the same peak, implying in a factor of multiplicity 6).

In order to get the expression for the intensity, we need three more correction factors: (a) Lorentz factor, (b) polarization factor, and (c) temperature factor. The first two are related to the geometric corrections that affect the diffracted intensity. Finally, the last one is related to temperature process that can cause shift in the position of the peaks, decreasing the intensity of the peaks and increasing the background.

A more complete explanation of the expression for the intensity and the factor that affects the intensity can be found in the reference of this chapter [52–57].

3.3. Experiment

The optics and the instrumentation used in the X-ray diffraction technique are directly related to the type of the X-ray source. However, we can define three generic elements: X-ray source, sample (including here the sample holder and sample environment, such as furnaces and cryostat), and detector.

An optimized experiment has as premise the following three conditions:

- Suitable X-ray source with efficient beam conditioning.
- A sample properly prepared, an optimized sample holder with low background and minimum influence in the measurement, and an appropriated sample environment that allows a stabilization of the sample in certain conditions as for example, temperature.
- Optimized detection systems (with or without optics to reduce background and to focus the scattered beam in order to improve the signal to noise ratio).

3.3.1. Experimental procedures of X-ray diffraction

The diffractograms show the diffracted intensities as a function of experimental parameter 2θ (angle between the diffracted and undeviated X-ray waves). The intensity is typically expressed in counts or counts per seconds while the peaks are listed as positions in degrees or in d -spacing (measured in Å or nm).

3.4. Crystalline materials

For materials with long ordering structure (crystalline materials) the diffractograms show sharp peaks, which the shape and the width depend on the instrument geometry where the data were collected. In **Figure 6**, we display an example of a diffractogram of a drug delivery system, β-cyclodextrin. The measurements were performed in a conventional diffractometer with Cu radiation, and, it was possible to perform a Rietveld refinement to obtain the final structure (as shown in the insert of **Figure 6**).

The range of the measurement for crystalline materials depends on the aim of the study. For example, when we study big molecules (for instance, biological samples), it is beneficial to measure at low angles, allowed by the geometry of the instrument (approximately 0.5° can be reached in a typical laboratory configuration in modern instruments or less than 0.5° using synchrotron sources).

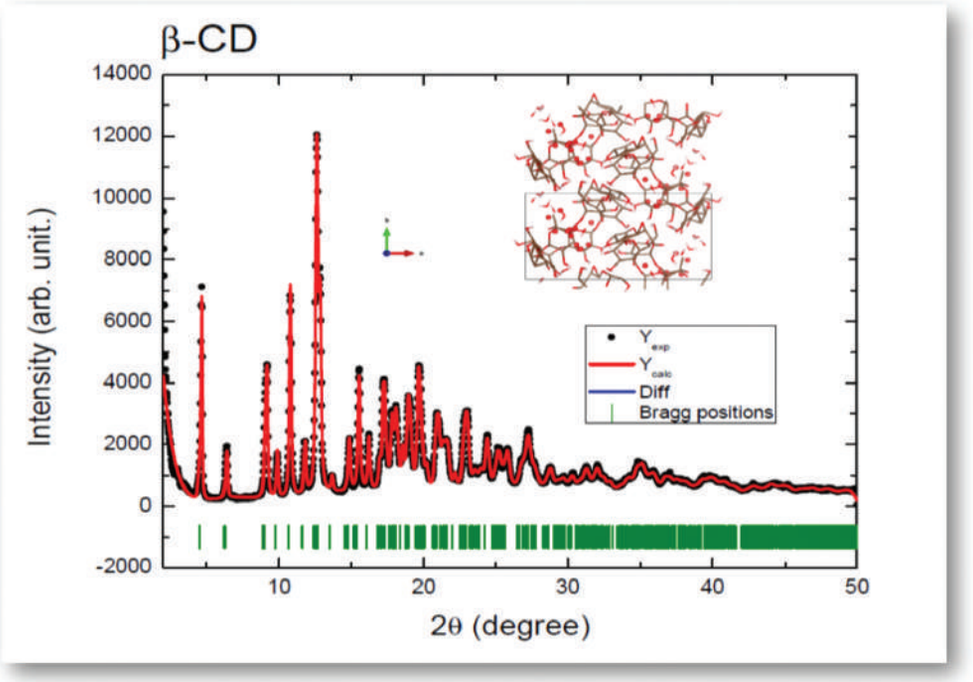

Figure 6. Diffractogram of crystalline β-cyclodextrin measured in a conventional diffractometer using Cu radiation. Also, Rietveld refinement was performed in order to obtain the crystal structure.

The time for collecting the data varies according to the application, for example, to study polymorphism in drugs. Good diffraction patterns of the crystalline material, using conventional X-ray instruments can be obtained in the range of 2–10 min per step. In configurations that use high efficiency X-ray sources (synchrotron) to samples mounted in a planar configuration, the collected time can be less than 1 min. The X-ray diffraction technique that is typically nondestructive (if the flux of X-ray is too high, we can observe the radiation damage effect that can affect the sample), needs 2–20 mg of sample, depending on the configuration geometry of the instrument and the application.

The quality of the sample and its correct preparation in order to perform the XRPD experiment influences significantly in the characterization or identification of the crystalline material. We can cite two factors related to the preparation of the sample that can affect the results:

1. Orientation of the crystallites: ideal sample has a big number of random oriented crystallites.
2. Statistics of particles orientation: the reproducibility of an X-ray pattern depends on the statistic of the particles orientation when the preferred orientation limits the degree in which the pattern represents the structure.

For these reasons, one must evaluate the statistics of the particle orientation and the degree of the preferred orientation before starting the identification and analysis.

The effect of the preferred orientation of the crystallites in a sample can be observed as the increase in the intensity on some of the peaks and the decrease in the intensity on others. The

http://dx.doi.org/10.5772/65326

variation of the intensity is proportional to the degree of preferred orientation. In some cases, the sample holder geometries of the diffractometer can also generate different set of relative intensities.

Using samples that show a relatively small number of crystallites results in a diffractogram with poor statistics. If the small population of the big crystallites does not represent all the possible orientations, the relative intensities will not be reproducible.

The effect of the preferred orientation on the particle orientation can be minimized by spinning the sample holder.

3.5. Amorphous materials

Amorphous materials (disorder, vitreous or amorphous materials) have characteristic diffractograms with large halos and do not show sharp peaks in the XRPD patterns. **Figure 7(c)** and **(d)** displays examples of a typical diffractogram of an amorphous material.

However, using suitable computational methods it is possible to extract structural information from this X-ray diffraction patterns. In this case, it is necessary a large angular range, typically from 1 to 100° in 2θ. Besides, the time to collect the data must be longer than the frequently

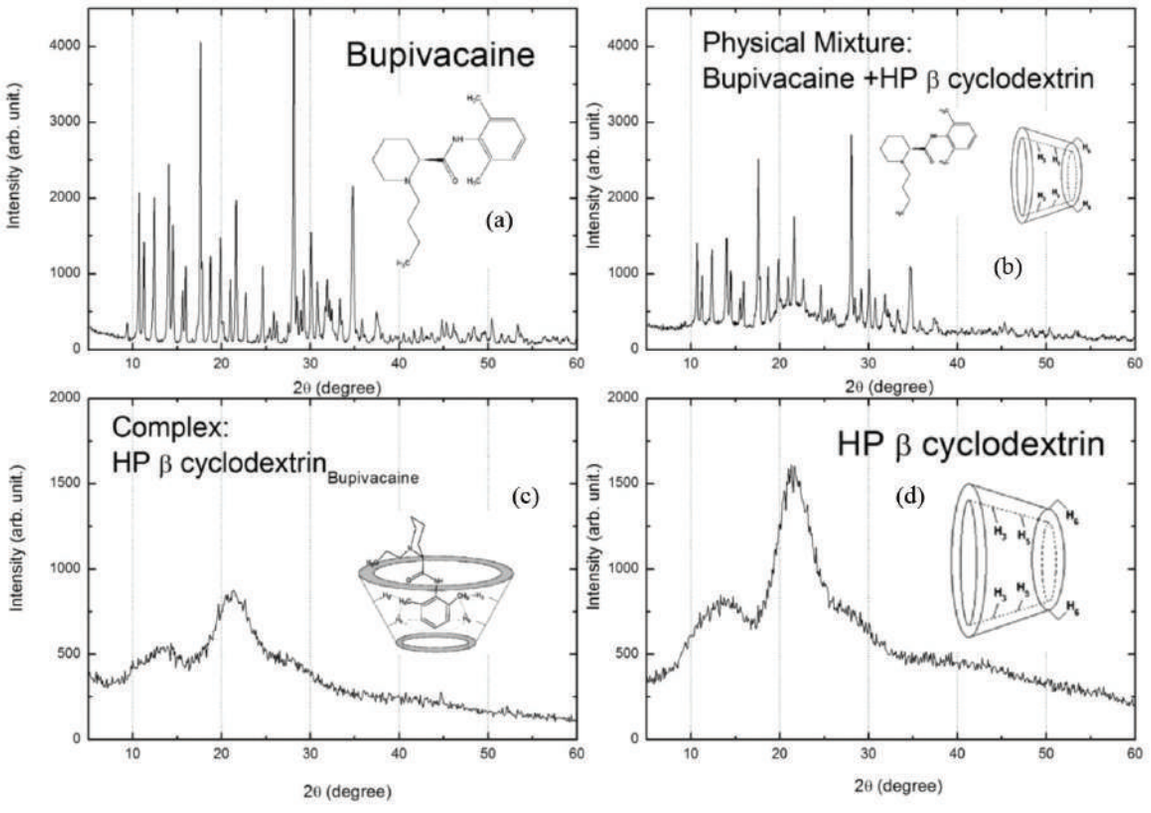

Figure 7. (a) Diffractogram of bupivacaine (BPV); (b) a physical mixture of BPV and HP-β-cyclodextrin; (c) complex of BPV and HP-β-cyclodextrin and (d) diffractogram of HP-β-cyclodextrin. Observe the amorphous diffractogram of the drug delivery systems, HP-β-cyclodextrin and the complex (drug delivery with drug).

used in conventional diffraction, due to the signal-noise ratio in an amorphous X-ray pattern be typically poor.

In order to obtain a good diffractogram through the X-ray diffraction technique for amorphous samples, usually one needs 5–100 mg of the samples, depending on the geometry of the instrument.

XRPD patterns, for crystalline materials or for amorphous materials, contain artifacts from the instrument, for example, background functions from the instrument, fingerprints from the sample holder, incoherent scattering (Compton), polarization and Lorenz effects, and air scattering. A relatively small pattern generated from the samples means that these artifacts represent a portion bigger of the overall diffracted intensity. Therefore, computational methods used to analyze amorphous materials are more sensitive to experimental artifacts.

3.6. Instrumentation

X-ray diffraction instrument used typically in conventional laboratories consists in three parts: (1) X-ray source; (2) sample holder, and (3) detector system.

There are several X-ray sources that it can be possible to use in a conventional laboratory, but the most common is the copper source (Cu). Slits and optics are used to focus the X-ray incident beam in the sample and also, the X-ray diffracted waves scattered from the sample into the X-ray detector. In order to minimize artifacts from the sample (mentioned before), usually, the sample holder is spinning. The X-ray detectors can be punctual, linear or area. The detector area has the advantage of being fast in the data acquisition and also makes it possible to evaluate the statistics of the particle orientation and preferred orientation of the samples, through the analysis of the Debye rings in the detector.

Synchrotron sources can be used to measure special systems in order to collect high quality data.

Diffractometers can be operated typically in reflection (Bragg-Brentano) or transmission (Debye-Scherrer). In the reflection setup, the incident beam is reflected from the surface of the sample and the scattered beam is focused into the detector.

The X-ray penetrates several layers below the surface in organic samples. This means that the average diffracted surface is located below the surface of the sample. This penetration effect can yield to an error of a displacement of the peak positions in the diffraction pattern of the tenth of a degree

Errors caused by the displacement of the peaks happen due to the difficulty in the preparation of the sample in the sample holder (**Figure 8(b)**). The surface of the sample must be leveled with the surface of the flat sample holder (where the instrument is focused). Although computational methods can be used to correct the position of the peaks, the proper preparation of the sample is the only solution to solve this problem.

http://dx.doi.org/10.5772/65326

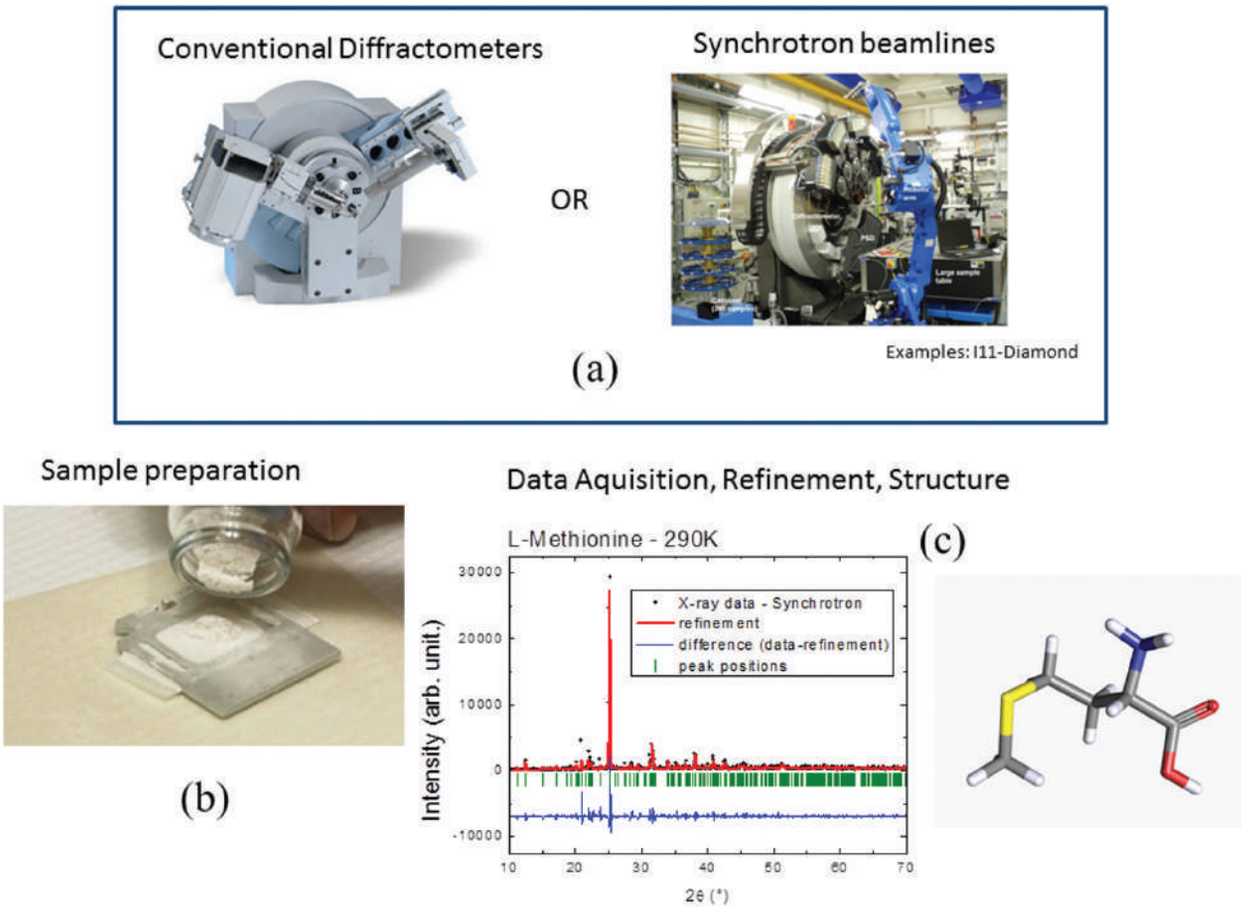

Figure 8. (a) Laboratory XRPD equipment or Synchrotron XRPD beamline can be used to characterize drug delivery systems and drugs; (b) preparation of samples; (c) some results from a biological material, L-methionine, measured at XRPD synchrotron beamline. Also observed the Rietveld refinement and the possible structure of the sample.

Usually measurement at low angles (below 2.5° in 2θ) is not appropriate due to the limitation of the instrument used mainly for big molecules, where it is expected to find reflections in the range from 0 to 2.5°. Measurements using the transmission setup can solve this limitation, when the instrument is properly set. In the transmission setup the X-ray incident beam pass through the sample. This configuration is possible for organic samples due to its relative transparence for X-rays. In this case, the sample does not need to be leveled with the sample holder surface, but the thickness of the sample is important and can cause errors in the displacement of the peaks. Besides, it is essential in this configuration that the sample holder is transparent to X-rays. In the case of amorphous materials, it is necessary an extra effort to operate the instrument in order to improve the quality of the data.

Acknowledgements

The authors acknowledge the financial support received by CNPq/Brazil and FAPESP (# grant 14/14457-5).

Author details

Margareth Kazuyo Kobayashi Dias Franco, Daniele Ribeiro de Araújo, Eneida de Paula, Leide Cavalcanti and Fabiano Yokaichiya

*Address all correspondence to: margareth_franco@yahoo.com.br; mkfranco@ipen.br

1 Brazilian Multipurpose Reactor, Nuclear and Energy Research Institute, IPEN, São Paulo, SP, Brazil

2 Human and Natural Sciences Center, Federal University of ABC, Santo André, SP, Brazil

3 Biochemistry and Tissue Biology Department, Biology Institute, State University of Campinas-Campinas, SP, Brazil

4 Chemical Engineering, State University of Campinas-Campinas, SP, Brazil

5 Department of Quantum Phenomena in Novel Materials, Helmholtz Zentrum Berlin, Berlin, Germany

References

[1] Neubert. Potentials of new nanocarriers for dermal and transdermal drug delivery. Eur. J. Pharm. Biopharm. 2011;77(1–2).

[2] Solarex. SX-40 & SX-50 Photovoltaic Modules [Internet]. http://www.trichord-inc.com/pricing/frames/content/solar_power.pdf. 1999

[3] Mc Grath S, van Sinderen D (editors). (2007). Bacteriophage: Genetics and Molecular Biology (1st ed.). Caister Academic Press. https://en.wikipedia.org/wiki/Bacteriophage(ISBN 978-1-904455-14-1)

[4] http://www.virology.wisc.edu/virusworld/images/cpv-half-nuc.jpg. 2014.

[5] Grass RN, Robert N, Athanassiou EK, Stark WJ.Covalently functionalized cobalt nanoparticles as a platform for magnetic separations in organic synthesis". Angew. Chem. Int. Ed. 2007;46(26): 490912. doi:10.1002/anie.200700613.https://en.wikipedia.org/wiki/Magnetic_nanoparticles.

[6] https://en.wikipedia.org/wiki/Nanoparticle#/media/File:Mesoporous_Silica_Nano-Particle.jpg. 2015.

[7] http://www.omicsonline.org/articles-images/2161-0398-2-105-g001.gif.

[8] http://www.foresight.org/Conference/MNT7/Papers/Cagin3/.

[9] http://cmb.gu.se/english/research/organic-and-medicinal-chemistry/Biomedical_Photonics/projects/gold-nanoparticles-.

[10] http://pubs.acs.org/doi/abs/10.1021/bm2010774.

[11] http://image.slidesharecdn.com/lipoproteins-150424045513-conversion-gate02/95/lipoproteins-8-638.jpg?cb=1429869399.

[12] http://www.pharmatutor.org/articles/nanocochleate-novel-bypass-of-conventional-drug-elivery-system.

[13] http://www.ebioscience.com/media/images/resources/knowledge-center/product-line/efluor/efluor-nc/nc-technology/efluor-nanocrystal-compostion.png.

[14] http://www.photonics.com/Article.aspx?AID=57396.

[15] http://blogs.nottingham.ac.uk/malaysiaknowledgetransfer/files/2013/06/Siva001.jpg.

[16] http://www.keystonenano.com/platform/liposomes.

[17] http://www.nature.com/nnano/journal/v3/n2/fig_tab/nnano.2008.13_F1.html.

[18] http://web.mit.edu/lms/www/images/Fig.%205B%20sm.jpg.

[19] http://www.carbonallotropes.com/carbon-nanotubes/39-single-wall-carbon-nanotubes.html.

[20] http://www.nature.com/nnano/journal/v2/n4/fig_tab/nnano.2007.90_F1.html.

[21] Oshiro A, da Silva DC, Santos ACM, Akkari ACS, de Araujo, Daniele R. Development of drug-delivery systems: strategies for new pharmaceutical formulations based on liposomal and micellar systems. Supramolecular Chemistry, Nanotechnology (1st ed.). São Paulo: Atheneu In: Alve WA. (Org.). 2014;vol.1; pp. 249–264.

[22] Holowka E, Bhatia SK. Drug Delivery, Material Design and Clinical Perspective. Springer-Verlag New York. 2014. ISBN 978-1-4939-1998-7, DOI: 10.1007/978-1-4939-1998-7

[23] Egelhaaf SU, Wehrli E, Muller M, Adrian M, Schurtenberger P. Determination of the size distribution of lecithin liposomes: A comparative study using freeze fracture, cryoelectron microscopy and dynamic light scattering. J. Microsc (Oxf). 1996;184:214–228. (ISSN 0022-2720)

[24] Evjen TJ, Hupfeld S, Barnert S, Fossheim S, Schubert R, Brandl M. Physicochemical characterization of liposomes after ultrasound exposure-mechanisms of drug release. J. Pharm. Biomed. Anal. 2013;78–79:118–122. DOI: 10.1016/j.jpba.2013.01.043

[25] Zuidam NJ, de Vrueh R, Crommelin Daan JA. (2003). Characterization of Liposomes In: Liposomes: A Practical Approach. Torchilin, Vladimir P, Weissig, Volkmar (eds). Oxford University Press, London (2nd ed.) pp. 31–78.

[26] Glatter O, Kratky O. Small Angle X-Ray Scattering. Academic Press, London. 1982.

[27] Glatter O. Scattering studies on colloids on biological interest (Amphiphilic Systems). Progr. Colloid. Polym. Sci. 1991;84:46–54.

[28] Kratky O. The world of neglected dimensions, SAS of X-ray and neutrons of biological macromolecules. Nova Acta Leopoldina NF 55; 1983.

[29] Trevisan J, Cavalcanti LP, Oliveira CLP, de la Torre L, Santana MH. Technological aspects and scalable enhanced processes for production of functional cationic liposomes as delivery system in gene therapy. In: Non-viral Gene Therapy. Yuan, X. (ed), Intech, Croatia OPEN ACCESS: http://dx.doi.org/10.5772/17869. (ISBN 978-953-307-538-9)

[30] Oliveira CLP, Gerbelli BB, Silva ERT, Nallet F, Navailles L, Oliveira EA, Pedersen JS. Gaussian deconvolution: A useful method for a form-free modeling of scattering data from mono- and multilayered planar systems. J. Appl. Crystallogr. 2012;45:1278−1286.

[31] http://www.azom.com/equipment-details.aspx?EquipID=3095. 2016.

[32] Brzustowicz MR, et al. X-ray scattering from unilamellar lipid vesicles. J. Appl. Cryst. 2005;15:38:126–131.

[33] Gasperini A, Puentes-Martinez X, Balbino T, Rigoletto T, Corrêa G, Cassago A, Portugal R, de La Torre LG, Cavalcanti LP. Association between cationic liposomes and low molecular weight hyaluronic acid. Langmuir (2015) 31:3308.

[34] Balbino TA, Gasperini AAM, Oliveira CLP, Azzoni A, Cavalcanti LP, de la Torre L. Correlation of the physico-chemical and structural properties of pDNA/cationic liposome complexes with their in vitro transfection. Langmuir. 2012;28:11535.

[35] Castelletto V, Parras P, Hamley IW, Bäverbäck P, Pedersen JS, Panine P. Wormlike micelle formation and flow alignment of a Pluronic block copolymer in aqueous solution. Langmuir. 2007;23(13):6896–6902.

[36] Artzner F, Geiger S, Olivier A, Allais C, Finet S, Agnely F. Interactions between poloxamers in aqueous solutions: Micellization and gelation studied by differential scanning calorimetry, small angle X-ray scattering, and rheology. Langmuir. 2007;23(9): 5085–5092.

[37] Alexandridis P, Hatton T. Poly(ethylene oxide)-poly(propylene oxide)-poly(ethylene oxide) block copolymer surfactants in aqueous solutions and at interfaces: Thermodynamics, structure, dynamics, and modeling. Coll. Surf. A: Physicochem. Eng. Asp. 1995;96:1–46.

[38] Santos Akkari AC, Ramos Campos EV, Keppler AF, Fraceto LF, de Paula E, Tófoli GR, de Araujo DR. Budesonide-hydroxypropyl-β-cyclodextrin inclusion complex in binary poloxamer 407/403 system for ulcerative colitis treatment: A physico-chemical study from micelles to hydrogels. Colloids. Surf. B: Biointerfaces. 2016;38:138–147.

[39] Oshiro A, da Silva DC, de Mello JC, de Moraes VW, Cavalcanti LP, Franco MK, Alkschbirs MI, Fraceto LF, Yokaichiya F, Rodrigues T, de AraujoDR. Pluronics f-127/l-

81 binary hydrogels as drug-delivery systems: Influence of physicochemical aspects on release kinetics and cytotoxicity. Langmuir. 2014;30(45):13689–13698.

[40] Mello JC, Moraes VW, Watashi CM, da Silva DC, Cavalcanti LP, Franco MK, Yokaichiya F, de Araujo DR, Rodrigues T. Enhancement of chlorpromazine antitumor activity by Pluronics F127/L81 nanostructured system against human multidrug resistant leukemia. Pharmacol. Res. 2016;111:102–112.

[41] Avachat AM, Parpani SS. Formulation and development of bicontinuous nanostructured liquid crystalline particles of efavirenz. Colloids. Surf. B: Biointerfaces. 2015;126:87–97.

[42] Chen Z, Liu Z, Qian F. Crystallization of bifonazole and acetaminophen within the matrix of semicrystalline, PEO-PPO-PEO triblock copolymers. Mol. Pharm. 2015;12(2): 590–599.

[43] Kopeček J, Yang J. Smart self-assembled hybrid hydrogel biomaterials. Angew. Chem. Int. Ed. Engl. 2012;51:7396–7417.

[44] Zhang L, Zhang N. How nanotechnology can enhance docetaxel therapy. Int. J. Nanomed. 2013;8:2927–2941.

[45] Ricardo NM, Ricardo NM, Costa Fde M, Bezerra FW, Chaibundit C, Hermida-Merino D, Greenland BW, Burattini S, Hamley IW, Nixon KS, Yeates SG. Effect of water-soluble polymers, polyethylene glycol and poly(vinylpyrrolidone), on the gelation of aqueous micellar solutions of Pluronic copolymer F127. J. Colloid. Interface. Sci. 2012;368(1):336–341.

[46] Nambam JS, Philip J. Thermogelling properties of triblock copolymers in the presence of hydrophilic Fe_3O_4 nanoparticles and surfactants. Langmuir. 2012;28(33):12044–12053.

[47] Kerkhofs S, Willhammar T, Van Den Noortgate H, Kirschhock CE, Breynaert E, Van Tendeloo G, Bals S, Martens JA. Self-assembly of Pluronic F127-silica spherical core-shell nanoparticles in cubic close-packed structures. Chem. Mater. 2015;27(15):5161–5169.

[48] Simões SM, Veiga F, Torres-Labandeira JJ, Ribeiro AC, Sandez-Macho MI, Concheiro A, Alvarez-Lorenzo C. Syringeable Pluronic-α-cyclodextrin supramolecular gels for sustained delivery of vancomycin. Eur. J. Pharm. Biopharm. 2012;80(1):103–112.

[49] Pradal C, Jack KS, Grøndahl L, Cooper-White JJ. Gelation kinetics and viscoelastic properties of Pluronic and α-cyclodextrin-based pseudopolyrotaxane hydrogels. Biomacromolecules. 2013;14(10):3780–3792.

[50] Shih KC, Li CY, Li WH, Lai HM. Fine structures of self-assembled beta-cyclodextrin/Pluronic in dilute and dense systems: A small angle X-ray scattering study. Soft. Matter. 2014;10(38):7606–7614.

[51] Wunderlich B. A classification of molecules and transitions as recognized by thermal analysis. Thermochim. Acta. 1999;340/41:37–52.

[52] Als-Nielsen J, McMorrow D. Elements of Modern X-ray Physics. Wiley, New York ; Chichester. 2001; xi:318 p.

[53] Cullity BD, Stock SR. Elements of X-ray Diffraction. Addison-Wesley Reading, MA. 1978

[54] Klug HP, Alexander LE. X-ray Diffraction Procedures for Polycrystalline and Amorphous Materials. Wiley, New York; 2nd ed, 1974; xxv:966 p.

[55] Warren BE. X-ray Diffraction. Dover Publications, New York, 1990; vii:381p.

[56] Young RA, The Rietveld Method (International Union of Crystallograhy Oxford University Press, [Chester, England] Oxford; New York, 1993; x: 298 p.

[57] Zachariasen WH, Theory of X-ray Diffraction in Crystals (J. Wiley and Sons, Inc. Chapman and Hall, Ltd, New York London, 1945;vi: 1 l 255 p.